Electrochimica Acta 451 (2023) 142299

Contents lists available at ScienceDirect

Electrochimica Acta

journal homepage: www.journals.elsevier.com/electrochimica-acta

Novel electrodeposited NiFeP/Zn bifunctional catalytic coating for alkaline water splitting

Jhaniel Osorio Silva, Santiago Cartagena, Jorge A. Calderón *

Centro de Investigación, Innovación y Desarrollo de Materiales – CIDEMAT, Universidad de Antioquia, Cr. 53 No 61 – 30, Torre 2, Lab. 330, Medellín, Colombia

ARTICLE INFO

Keywords:
Hydrogen evolution
Oxygen evolution
Water electrolysis
NiFeP/Zn catalysts
Electrodeposited coatings
Corrosion

ABSTRACT

The shift towards renewable energies has promoted research into electrolysis for the obtention of pure hydrogen since this is a promising energy vector. However, electrolysis is limited due to its low efficiency. In this work, a novel NiFeP/Zn coating electrodeposited on AISI 304 steel is proposed as a bifunctional catalytic electrode for electrochemical water splitting. The leaching of Zn from the coating allows the formation of a diversified surface morphology of the electrode, obtaining an active area 1164 times greater than that of a NiFeP coating. The leaching process also allows the formation of Ni oxides, hydroxides and oxyhydroxides, which are beneficial catalytic compounds for the reactions of interest. XRD characterization indicates the presence of an amorphous structure of the coating due to the presence of P, which provides better catalytic performance for the hydrogen evolution reaction (HER) and oxygen evolution reaction (OER), as well as better corrosion behavior of the electrodes. The electrocatalytic performance of the coating shows overpotentials of 163 mV for HER, and 262 mV for OER in 1 M NaOH at |10| $mAcm^{-2}$. The full cell test using the NiFeP/Zn coating as bifunctional electrode shows a remarkably low overpotential equal to 1.65 V at 10 mA cm^{-2} for overall water splitting.

1. Introduction

The environmental impact and health issues generated by the increasing amounts of pollutants and gasses such as CO, CO_2, NO_X, SO_2, etc. produced by the use of fossil fuels, had led to a growing interest in the research and development of clean energies sources [1]. However, renewable sources of energy such as wind and solar present an intermittent nature, making storage a necessity to provide constant energy. In this respect, hydrogen has some interesting characteristics for use as an energy vector and to store energy, including good energetic density by mass and the fact that only water is produced as a result of its combustion, making it suitable for the necessary transition [2,3]. Hydrogen can be used not only for energy purposes, it is also very important for the decarbonization of big industries such as steel and fertilizer production [4–6]. Hydrogen can be obtained through water electrolysis, which is a process used to transform electricity in hydrogen using the splitting of the water molecule to obtain oxygen and hydrogen gasses according to the reaction $2H_2O \rightarrow 2H_2 + O_2$. Electrolysis in alkaline media is cheaper than in an acid media because it is not necessary to use scarce materials such as Pt, Ru, or Ir. Nevertheless, to enable the proliferation of electrolysis for hydrogen production by allowing it to compete with other clean and more industrially-established storage systems such as ion-lithium batteries, it is necessary to address two issues: ohmic losses in the process and the reduction of the cost of materials used in electrolysis [7–9].

The development of novel materials through surface modification of the electrodes used in electrolysis aims to solve the two drawbacks mentioned above, because the use of an electrocatalyst coating makes it possible to obtain greater reaction efficiencies by improving electrolyte-electrode interactions [10], and to obtain materials with good corrosion performance [11,12]. To achieve this, it is necessary to find materials that can reduced the overpotentials associated with the hydrogen evolution reaction (HER) and the oxygen evolution reaction (OER) and facilitate good coating stability for long periods. Different materials have been studied and analyzed in order to understand these interactions, but the most commonly-used materials are nickel-based alloys, due to their great catalytic properties associated with the formation of oxides, hydroxides and oxyhydroxides on the surface in alkaline pH [13]. Among these nickel-based alloys, NiFe are widely used for tribological, corrosive and catalytic improvement of different substrates [11, 14–16]. The inclusion of phosphorus in these alloys to form a ternary NiFeP system has been investigated by methods such as electroless

* Corresponding author.
E-mail address: andres.calderon@udea.edu.co (J.A. Calderón).

https://doi.org/10.1016/j.electacta.2023.142299
Received 13 September 2022; Received in revised form 27 March 2023; Accepted 27 March 2023
Available online 27 March 2023

plating [13], hydrothermal deposition [17–19] and electrodeposition [20–23]. With the addition of P in the electrochemical bath, it is possible to reduce the anomalous deposition presented in NiFe alloys electrodeposition and promote the growth of an amorphous structure within the coating, which helps improve the corrosion resistance and the catalytic properties of the deposit [14]. Meanwhile, the inclusion of zinc in the coating, to form a ternary NiFeZn system, has allowed enhancement of the catalytic properties through the generation of high surface area materials, due to cracks and pores formed in the process of zinc leaching, increasing the contact zone of the surface and improving the interactions of the electrode with the electrolyte [14,24–26].

Some authors have worked with techniques that seek to improve the results of nickel-based coatings by simplifying the obtention process and varying the architecture of the electrode. Some techniques involved the use of flat electrodes to obtain inexpensive catalysts, and others the use of meshes and foams to obtain 3D catalysts and create a greater surface area. Previously, there was a focus on developing just one of the water splitting reactions. For example, Roy et al. worked on water oxidation (OER) with an electrodeposited $NiFeO_xH_y$ system that required just ~290 mV to achieve 10 mA cm^{-2} [27]. An enhanced system doped with Zn to form Zn:$NiFeO_xHy$ was developed by Lim et al., reaching values of ~250 mV at 10 $mAcm^{-2}$ for the same reaction [28]. Meanwhile, for the hydrogen evolution reaction, Bachvarov and co-workers electrodeposited amorphous systems of NiFeCo, with 120 mV at 10 mA cm^{-2}, and NiFeCoP, with 78 mV at 10 $mAcm^{-2}$, achieving an important reduction in the kinetics of HER in comparison to an Ni electrode [29]. Yang et al. used Ni foam substrate to obtain a NiCoP coating that resulted in a low overpotential of approximately 107 mV for HER at 10 $mAcm^{-2}$ in a KOH system [30]. An NiCo/Zn electrodeposited system that was leached to remove part of the Zn was developed by Herraiz-Cardona et al., which resulted in an enhancement related to the greater surface area, obtaining 119.6 mV at 100 $mAcm^{-2}$ [26]. Currently there is an increasing interest in developing materials that have good performance for both reactions, thereby making scalable the process of the catalysts' deposition. For example, Sankaran et al. developed a bifunctional Ni+YSZ catalyst with overpotentials of 131 mV for HER and 331 mV for OER at |10| $mAcm^{-2}$, using the atmospheric plasma spray (APS) technique and modifying the deposition with an aluminum mesh to obtain greater surface area [31]. Other examples, but using hydrothermal deposition, are Ramakrishnan et al., who developed an interesting $NiSe_2$ catalyst on nickel foams to obtain 175 mV at |10| $mAcm^{-2}$ for HER and 325 mV at |50| $mAcm^{-2}$ for OER [32]; and Diao et al., who obtained a NiFeP/NiP/NF system, achieving overpotentials of 105 mV for HER and 227 mV for OER at |10| $mAcm^{-2}$ [17]. Some of the previous results obtained with meshes and foams are significantly catalytic, but analysis of these systems is very difficult, because it is not possible to fully identify and isolate the individual contributions provided by the reactions on the catalyst and on the substrate [33].

Based on the previous considerations, and with the intention of obtaining electrocatalytic surfaces for bifunctional electrodes with low cost and low overpotential (η) in the electrolysis reaction, this work proposes the formation of catalytic coatings of NiFeP/Zn after the leaching of Zn from a NiFePZn quaternary system deposited on AISI-SAE 304 stainless steel substrates by means of room temperature electrodeposition. The aim of this procedure was to obtain catalytic surfaces with high surface area for the electrolysis of water in an alkaline medium and a reduction in costs in the development of the electrodes. Furthermore, the proposed process does not require high temperatures to produce the catalyst and can be easily scalable at an industrial level.

2. Experimental procedure

2.1. Electrode preparation and NiFeP/Zn coating obtention

AISI 304 stainless steel was used as substrate for the electrode preparation. This was covered with epoxy resin, leaving a defined area for the subsequent electrochemical analysis and evaluation. The exposed area was polished with sandpaper from P600 up to P2000 grit, in order to obtain a more homogenous surface. After an appropriate cleaning process with ethanol in ultrasonic bath for five minutes, the electrodes were subjected to anodic treatment in an aqueous solution with 10% v/v sulfuric acid (J.T. Baker® 95.9%) and 10% v/v glycerol (pharmaceutical grade) for 10 min at a current density of 1 A cm^{-2}, in order to enhance the surface area and the adherence of the coating. Finally, the electrodes were washed with abundant distillate water [34,35].

NiFePZn coatings were electrodeposited using Pt foil as counter electrode and applying a current density of – 40 $mAcm^{-2}$ to the working electrode for 2400 s. The electrolytic bath was made up of distilled water with 0.114 M $NiSO_4{\cdot}6H_2O$ (EMSURE® MERK, ≥ 99.0%), 0.108 M $FeSO_4{\cdot}7H_2O$ (CARLO ERBA, ≥ 99.5%), 0.102 M CH_3COOK (EMSURE® MERK, ≥ 99.0%), 0.094 M $NaH_2PO_2{\cdot}H_2O$ (ALDRICH, ≥99%). Variations of the amount of $ZnSO_4{\cdot}7H_2O$ contained in the electrolytic bath were performed to obtain various quaternary coatings. The variation range of $ZnSO_4{\cdot}7H_2O$ was defined between 1.4 mM and 8.4 mM with increases of 1.4 mM. The pH of the bath was adjusted to a value of 2 with sulfuric acid additions for better Fe^{2+} stability and phosphorous behavior [21]. Agitation of the bath was generated through air bubbles. After the electrodeposition, all the electrodes with various Zn concentrations were treated with 6.0 M NaOH for 24 h at room temperature in order to leach the deposited Zn and generate the final NiFeP/Zn coatings. After that, distillate water was used to rinse the electrodes.

2.2. Materials characterization

The morphology of the NiFePZn coatings and the effect of leaching Zn from the electrodes to form NiFeP/Zn, were characterized by scanning electron microscopy (SEM) and electron dispersive X-ray spectroscopy (EDS), using a JEOL-JSM 6490LV device with accelerating voltage of 20 kV. As a complement to the surface morphology observation of the deposited coating, an analysis was made with an Asylum Research Atomic Force Microscope (AFM) from OXFORD Instruments. Chemical composition was evaluated through Raman spectroscopy, using a Horiba Jobin Yvon (Labram HR) Nikon (BX41) microscope with a CCD detector (Wright 1024 × 256 pixels) with a laser of 625 nm; and X-ray photoelectron spectroscopy (XPS), with a (NAP-XPS) spectrometer with a PHOIBOS 150 1D-DLD analyzer, using a monochromatic source of Al-Kα (1486.7 eV, 13 kV, 100 W) with step energy of 90 eV for general spectra and 20 eV for high resolution spectra. Crystal structures were characterized by X-ray diffraction (XRD) with a Miniflex600 Rigaku with CuK_α (λ=1.54059 Å) as source, operated with a source power of 40 kV and 15 mA from a 2θ from 10° to 80°.

2.3. Electrochemical evaluation

Electrochemical experiments were carried out in 1.0 M NaOH for HER and OER and were performed using a potentiostat/galvanostat AUTOLAB PGSTAT302F, while the electrochemical impedance spectra (EIS) were made using a Zhaner IM6e potentiostat. The electrolyte used was 1 M NaOH. A H-type cell, with a distance between the anode and cathode electrodes of approximately 10 cm and an electrolyte volume of 80 cm^3 was used for all measurements. A Hg|HgO electrode, made in-house, was used as reference electrode and a Pt mesh was used as counter electrode. Precautions were taken to avoid possible interference from platinum ions released by the counter electrode during HER experiments. Specifically, for short LSV measurements (ca. 3 min), we used an electrochemical cell with a porous polypropylene membrane, which acted as a physical separator between the anodic and cathodic compartments of the cell. Fresh electrolyte was used for each of these electrochemical measurements. In the case of long-term stability experiments, such as the measurements of overpotential vs time, a flow cell was used to avoid the accumulation of bubbles and a graphite slab was used as counter electrode.

Potentials with respect to reversible hydrogen electrode were calculated as follows [23]:

$$\eta = \varepsilon_m + \varepsilon_{ref/H2} + (0.059V \times pH) - (R_{sln} \times I) \quad (1)$$

Where, ε_m is the measured potential, $\varepsilon_{ref/H2}$ is the potential difference between the reference electrode and the reversible hydrogen electrode (RHE), I is the response current of the measurement at the working electrode and the R_{sln} is the solution resistance obtained with a current interrupt (iR) measurement and using EIS.

Linear sweep voltammograms (LSV) were performed in three different samples (in order to verify reproducibility) from 0.20 V to 1.10 V for OER and from −0.40 V to −1.80 V for HER at a scan rate of 5 mV s^{-1}. Subsequently, cyclic voltammetry at a low scan rate of 0.1 V s^{-1} was performed from 0.20 V to 0.70 V and −0.90 V to −1.40 V to check the stability of the surfaces of the samples. Further analysis of the stability and durability of the electrodes was done by chronopotentiometry measurements at a high current density of 400 mA cm^{-2} for 24 h, which is a typical condition for the real operation of an electrolyzer. Tafel plots were constructed from potentiodynamic polarization measurements made at 80 μV s^{-1} and a rotation speed of 3500 RPM using a rotating disk electrode. This was done to avoid shielding of the electrode surface due to bubble formation. The catalyst and the electrodes were prepared using the same methodology described previously.

The morphology factor (φ) of the NiFeP/Zn electrodes was evaluated from capacitance values extracted from cyclic voltammetry measurements performed in a potential window near to the open circuit potential (OCP). These showed clear capacitive behavior. 22 consecutive scan rates with 10 cycles per speed to obtain constant values were performed. The method used was based on previous investigations by Da Silva et al. [36] and Trasatti et al. [37]. With this methodology is possible to make a linear fitting to the curve of current density (j) vs scan rate and to establish the "internal" ($C_{D,i}$) and "external" ($C_{D,e}$) differential capacitances, using the slopes of the two linear segments. For low scan rate domain the current capacity follows Eq. (2), where (C_D) is the total differential capacity, and for high scan rate domain it follows Eq. (3), where $i_{C,r}$ is the capacitive current when scan rate tends to 0. The additive character of the current densities and capacitances expressed in Eqs. (4) and 5 is also valid. Consequently, the internal differential capacity can be calculated, as expressed by Eq. (5).

$$i_C = C_D v \quad (2)$$

$$i_C = i_{C,r} + C_D v \quad (3)$$

$$i_C = i_{C,i} + i_{C,e} \quad (4)$$

$$C_{D,i} = C_D - C_{D,e} \quad (5)$$

$C_{D,i}$ is related to the inner surface charge associated with the less accessible surface regions, such as pores, cracks, grain boundaries, etc. Finally, to calculate the morphology factor (φ), the ratio between the internal and the total differential capacitances must be considered, according to Eq. (6), which gives a value that can vary between 0 and 1.

$$\varphi = \frac{C_{D,i}}{C_D} \quad (6)$$

The evaluation of the corrosion performance (or durability) of the coatings in 1.0 M NaOH was carried out in two ways. The first of these comprised OCP monitoring, just after the end of polarization step, for a period of 3 h approximately, and then EIS measurements performed at the OCP with a perturbation amplitude of 10 mV and a frequency range from 100 kHz to 10 mHz. The OCP and EIS measurements were performed after 2 h of anodic polarization at 400 mA cm^{-2}, a process that was repeated until completing a total polarization time of 24 h, through ON/OFF cycles, which resembles the operation conditions when the electrodes are used in electrolyzers powered by intermittent energy sources. The second test to evaluate the corrosion behavior of the electrodes comprised LSV measurements performed before and after the complete cycles of polarization/OCP/EIS evaluation, to verify if there was a variation in the catalytic properties of the coatings.

3. Results and discussion

3.1. NiFeP/Zn coatings optimization

To increase the electroactive surface area of the electrodes, Zn was initially co-deposited on the anodic treated steel, together with the catalytic layer of NiFeP, to obtain NiFePZn which was then selectively dissolved to form NiFeP/Zn. A larger electroactive area is expected to be achieved due to the porosity or vacancies left by the dissolved Zn. To achieve this, a well-known electrolytic baths with the addition of different amounts of Zn were used to produce the catalytic NiFeP/Zn systems [23]. Details of process are presented in the experimental section. To determine the best electrocatalytic coating, linear sweep voltammograms (LSV), capacitance measurements and Raman spectra were considered. The catalytic performance of the coatings for HER and OER were studied using LSV, and the results are presented in Fig. 1. Fig 1 shows the effect of the amount of Zn contained in the electrodeposition bath on the catalytic performance of the obtained coatings. It is expected that a larger concentration of Zn in the bath will produce a larger amount of Zn in the NiFePZn catalytic layer that can be leached to form more cavities in the NiFeP/Zn. A decrease in the HER and OER overpotentials with the increase in Zn was observed, until Zn concentration in the electrodeposition bath reached a value of 7 mM, see Fig. 1c and d. Larger amounts of Zn than 7 mM produced an increment in the overpotential for both HER and OER. As expected, a larger electroactive area of the electrodes is achieved with the increase of Zn amount in the coating, due to the interconnected pores and greater surface roughness produced by the Zn dissolution process [24,26,38].

The overpotentials obtained at |10|, |30| and |100| mA cm^{-2} for HER and OER are presented in Table S1 in the supporting information. As mentioned above, the overpotentials were reduced with the increase of Zn concentration in the electrodeposition bath for the three current densities reported. However, there is a more significant enhancement when the middle concentration of Zn in the bath (after 4.2 mM of Zn in the bath) is deposited, a trend that is clearer for OER data than for HER data. The best overpotential values achieved for HER at |30| mA cm^{-2} and |100| mAcm^{-2} were 240 mV and 298 mV, respectively (Fig. 1a,c). Meanwhile, for OER the best values at |30| mA cm^{-2} and |100| mA cm^{-2} were 286 mV and 313 mV, respectively (Fig. 1b,d). We associate this behavior with the expected surface area increase as more Zn is leached from the surface. Zn concentration in the electrodeposition bath larger than 7 mM is not convenient because it produces large overpotentials for both HER and OER, possibly due to the excess of Zn electro-dissolution and loss of the catalytic layer, which leaves the steel substrate freely exposed. The best catalytic result obtained for the NiFeP/Zn coatings was compared with that obtained for a previously developed NiFeP coating (Zn-free coating) [23], in order to verify the beneficial effect of Zn co-deposition and posterior dissolution. This comparison is shown in Fig. 2. The inclusion of Zn and its subsequent leaching from the catalytic coating reduces the overpotential, compared to the reference free-Zn coating, by approximately 165 mV for HER and 62 mV for OER at |10| mA cm^{-2}, and 137 mV for HER and 70 mV for OER at |100| mA cm^{-2}.

The morphology factor (φ) was evaluated following the previous works of Da Silva et al. [36] and Trasatti et al. [37], who applied a method that can determine the differential response of the diverse morphology or topography of the catalytic-layer surface. This method was chosen to avoid the comparison between the actual experimental capacity and the reference capacity values, which is usual in current research in order to obtain the roughness factor (R_f) and establish the contribution of the electrochemical active surface area (ECSA) [23,39,

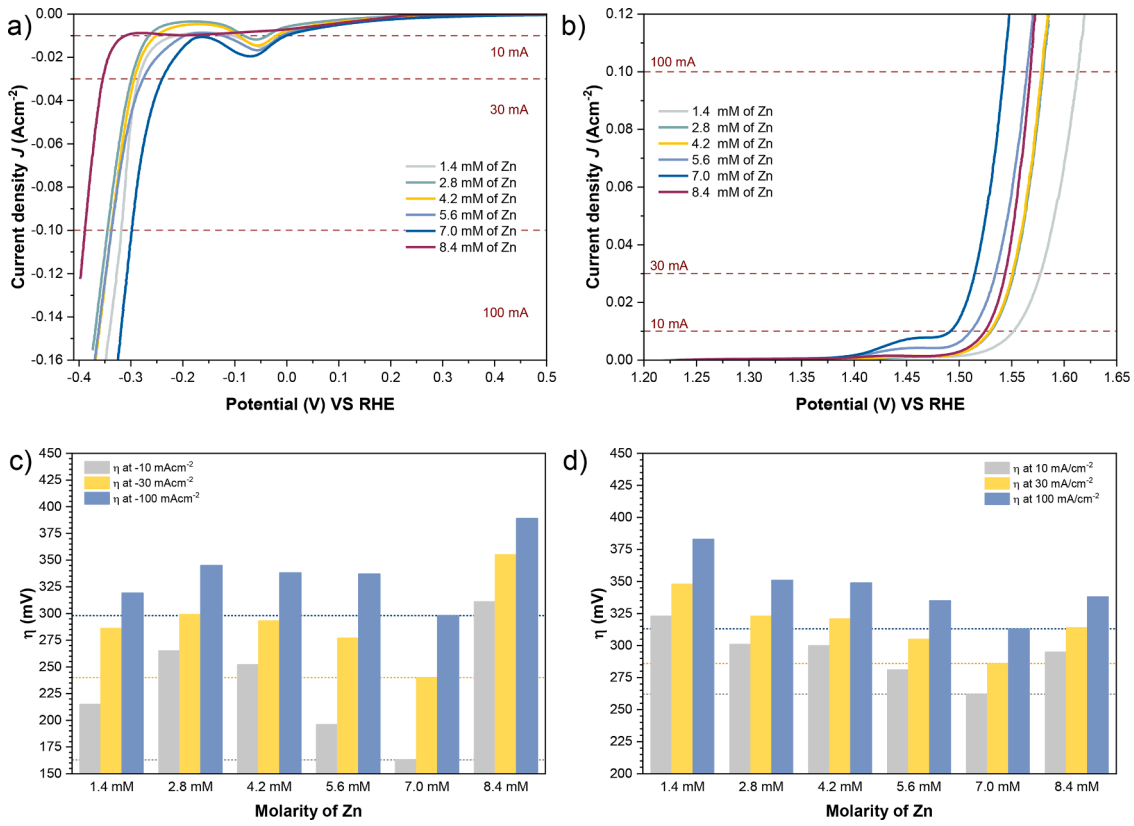

Fig. 1. Linear sweep voltammograms results for NiFeP/Zn coatings with Zn concentration variation (1.0 M NaOH). a) Cathodic evaluation for HER, b) Anodic evaluation for OER, c) cathodic overpotential obtained for HER and d) Anodic overpotential obtained for OER.

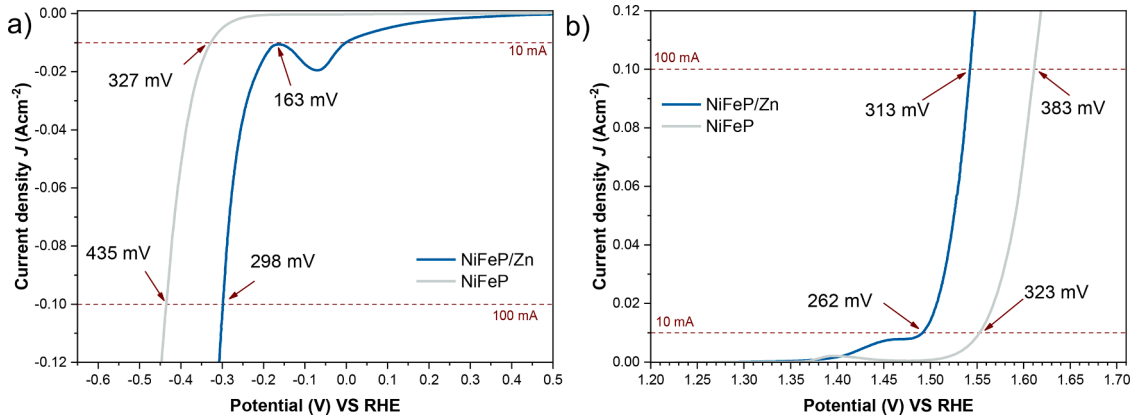

Fig. 2. Linear sweep voltammograms for the best NiFeP/Zn coating (7 mM of Zn) vs a NiFeP coating (1.0 M NaOH). a) Cathodic LSV evaluation (HER) and b) Anodic LSV evaluation (OER).

40]. Thus, the proposed methodology can decrease the possibility of wrong interpretations since it is difficult to obtain valid reference capacity values in order to compare exactly similar materials. This is because the reference capacity has only empirical validity, especially when the surface is quite heterogenous in nature, as is the case for metal oxides mixtures, making the analysis independent of the chemical nature of the species evaluated [36]. Cyclic voltammograms at different scan rates for NiFeP/Zn coatings with different initial Zn contents were performed in a potential range where capacitive behavior was observed. The CV plots performed in a potential window of ± 100 mV around the OCP are shown in Fig. S1 in the supporting information. Plots of the current density (*j*) vs scan rate obtained at 0.3 V vs RHE are shown in Fig. 3. All graphs clearly present two linear segments with different slopes, located at the low and high sweep rate domains. When the Zn content in the coating is low, the slopes are nearly identical, resulting in a low morphology factor for the electrocatalytic coating, as can be seen in Table 1. Table 1 also shows the corresponding data for the NiFeP coating (coating without initially Zn electrodeposition), for comparison purposes. A low φ value can be associated with low interconnected porosity and low surface inhomogeneities generated by the scarce Zn dissolution process. Consequently, when the Zn content in the coating is low the total differential capacity value is similar to the external capacity (low value of internal capacity) of the catalyst. On the other hand, when the Zn amount is large the two slopes observed in the plots of Fig 3 are quite different and a heterogenous topography with more irregular surface and interconnected porosity is achieved. In that case, the

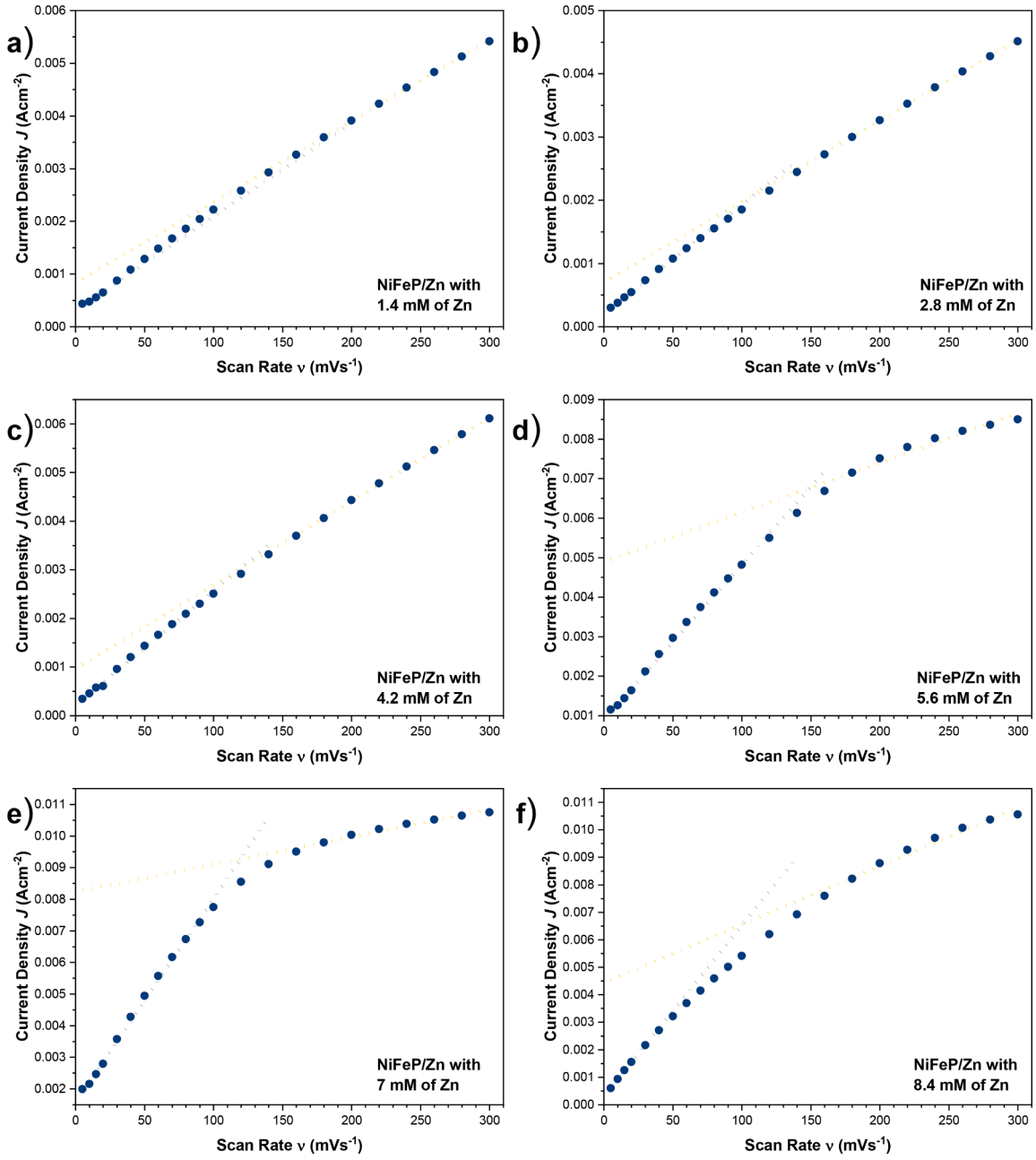

Fig. 3. Current Density (j) vs Scan Rate curves obtained through CV for a) 1.4 mM, b) 2.8 mM, c) 4.2 mM, d) 5.6 mM, e) 7 mM and f), 8.4 mM of Zn.

Table 1
Estimated capacitances and φ values of the coatings obtained using CV measurements.

Coating	C_D (Fcm^{-2})	$C_{D,e}$ (Fcm^{-2})	$C_{D,i}$ (Fcm^{-2})	φ
NiFeP	2.7819E-4	1.3592E-4	1.42227	0.5114
1.4 mM of Zn	1.7806E-2	1.5347E-2	2.4595E-3	0.1381
2.8 mM of Zn	1.7269E-2	1.2781E-2	4.4883E-3	0.2599
4.2 mM of Zn	2.3553E-2	1.7227E-2	6.3263E-3	0.2686
5.6 mM of Zn	3.9333E-2	1.2527E-2	2.6805E-2	0.6815
7 mM of Zn	6.4602E-2	8.6802E-3	5.5922E-2	0.8656
8.4 mM of Zn	6.2117E-2	2.1263E-2	4.0853E-2	0.6576

internal capacity can be differentiated from the external capacity and the morphology factor is large. Consequently, a large electroactive area of the catalyst is expected. According to the analysis performed by Da Silva et al. [36], during the CV experiments to calculate the coating capacitance, a fast ionic charging process, to satisfy the surface electroneutrality, occurs in the more external regions of the film, particularly the more easily accessible external regions. However, a slower ionic charging process happens in porous or irregular surfaces because they are regions of difficult access. Consequently, the internal capacity is only measurable in porous or irregular surface tested at low scan rates, as was corroborated in Fig. 3. The φ of the coating was observed to increase until the Zn concentration in the electrodeposition bath reached 7 mM, after which further increment of Zn does not produce increment in φ. The morphology factor values obtained from CV measurements and estimated capacitances are coherent with the catalytic behavior of the coating observed in the LSV curves, Figs. 1 and 2. The increment of the catalytic properties of the NiFeP/Zn coatings is consistent with the increment of the φ values, which indicates that large ECSA is achieved when morphology factor value is large, and consequently better catalytic performance of the coating is obtained.

Raman spectroscopy measurements were done to determine the

chemical changes of the NiFeP/Zn coatings before and after OER polarization. Ex-situ and in-situ Raman spectra obtained for the different coatings are shown in Fig. 4(a) and Fig. 4(b) respectively. The ex-situ Raman spectra of samples performed before electrolysis exhibited bands at 395 cm^{-1}, associated with the α-Fe_2O_3 compound [41], and at 680 cm^{-1}, which corresponds to NiO [42] and Fe_3O_4 oxides [41] which overlap with the formation of the band. The Raman spectrum obtained for the coating prepared with 8.4 mM of Zn, unlike the others, displays an absence of bands related with nickel or iron oxides, which indicates a metallic character of the surface, probably due to the substrate exposure. This result is in accordance with previous LSV test results, which indicated low catalytic performance of the coating prepared with 8.4 mM of Zn, possibly due to the exposure of the substrate after the leaching process.

The in-situ Raman spectra (Fig. 4(b)) were obtained during polarization of the samples at 0.6 V vs Hg|HgO. These spectra, like those obtained before electrolysis, display the previously described bands at 395 cm^{-1} and at 680 cm^{-1}. In addition, the presence of new bands at 475 cm^{-1} and 555 cm^{-1} was observed. These bands are characteristic of the vibrational responses of nickel oxyhydroxide (NiOOH) [42], which were formed due to the stimulus of the electrolysis process. The distortion that occurs in both bands is related to a disordered participation of Ni-Fe when the Fe concentration is above 32%, as Marie W. et al. have proposed [42]. That work also found that the increase of the intensity of the band at 555 cm^{-1} occurs with the increase of the Fe concentration in the deposit, until the bands reach a similar intensity. When Fe concentration in the deposit exceeds 40%, the catalytic capacity of the NiOOH species is reduced. A comparison of relative intensities of the bands at 475 cm^{-1} and 555 cm^{-1} (I_{475}/I_{555}) of the Raman spectra of the coatings was made and the results are presented in Table S2 in the supporting information. It can be clearly observed that I_{475}/I_{555} ratio increases as the initial Zn content in the deposited increases. This result suggests that the iron content in the catalytic layer concomitantly decreases in the deposits with initial high contents of zinc. After the leaching process, the coatings that initially have low Zn content could present iron enrichment, while the coating with high Zn content, like those obtained at 5.6 and 7 mM of Zn, could exhibit low iron content and Ni enrichment. According to these results, it is expected that the coating obtained at 7 mM of Zn will be the coating with the best Ni/Fe ratio (high Ni and low Fe contents) and the best catalytic activity to water splitting, because it was the coating that exhibited the highest I_{475}/I_{555} ratio in the Raman spectra. These results are coherent with the results obtained in the LSV and CV analyses, where the 7 mM of Zn coating is the one with the best electrochemical performance.

From the LSV, CV and Raman results previously analyzed, it can be established that the optimal coating, in terms of composition and catalytic behavior, is the one deposited with 7 mM of $ZnSO_4{\cdot}7H_2O$ in the bath. It is important to note that the incorporation of Zn, even in small amounts, leads to an important decrease in the HER and OER overpotentials. It appears that when Zn is leached from the coating, in addition to the generation of cavities, peaks and valleys, there are also convenient interactions between the other metals of the system, changing the proportions between Ni and Fe in the deposit, thereby improving the ratio of the compounds of both metals. The leaching process at high concentrations of NaOH makes it possible to reduce part of the deposited iron, bringing more optimal amounts of Ni and Fe in the deposit for the hydrogen and oxygen evolution reactions. In general, the leaching of zinc from the coating in alkaline medium not only generates an increase in the surface area but could also be considered an aging treatment that favors the reactions of interest.

3.2. Optimal NiFeP/Zn coating characterization

For a better understanding of the selected optimal coating from the previous analysis (NiFeP/Zn 7 mM of Zn), more exhaustive physical and chemical characterizations were carried out on that coating in order to define the microstructure, morphology and possible compounds formed by the elements present on the catalytic surface and the changes induced by the leaching process. The results obtained by scanning electron microscope (SEM) analysis are presented in Fig. 5. The micrograph

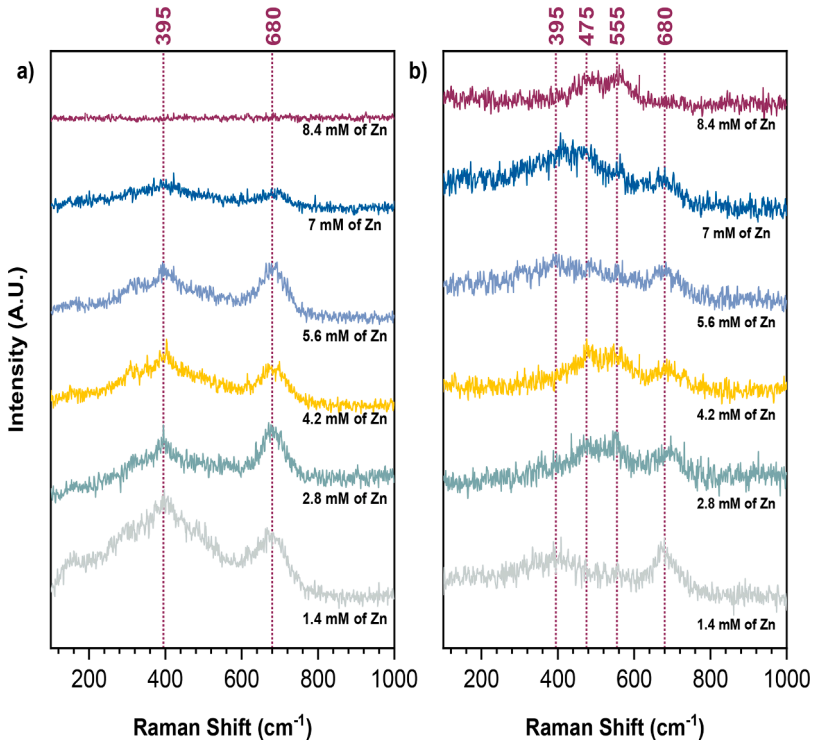

Fig. 4. Raman spectra obtained for the different leached NiFeP/Zn coatings. a) Ex-situ Raman spectra before electrolysis and b) In-situ Raman spectra during electrolysis at 0.6 V vs Hg|HgO.

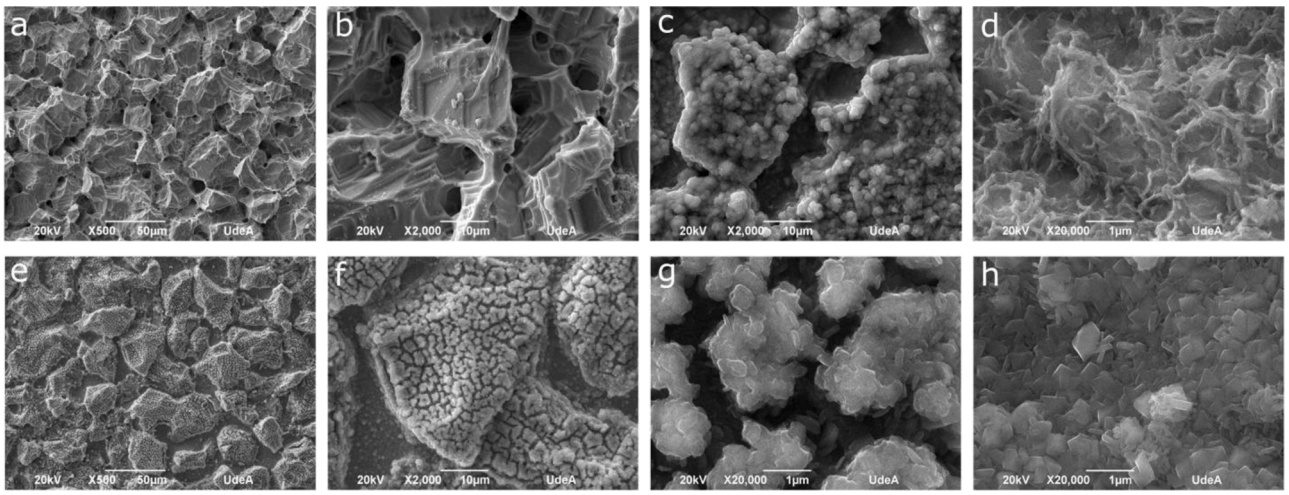

Fig. 5. SEM micrograph for electrodes surfaces. a) Anodic treated AISI 304 steel, b) NiFeP coated electrode, c) Unleached NiFePZn coated electrode at X2000 and d) Unleached NiFePZn coated electrode at X20000, e) Leached NiFeP/Zn coated electrode at X500, f) Leached NiFeP/Zn coated electrode at X2000, g) Leached NiFeP/Zn coated electrode at X20000 and h) Leached NiFeP/Zn coated electrode at X20000.

obtained for the substrate is shown in Fig. 5(a) where the AISI 304 steel after the anodic treatment can be observed. Some quite angular peaks and valleys are notable, and these lead to the formation of pores with sizes between 5 and 50 µm. The pores tend to form at the grain boundaries of the material due to the dissolution of Fe, which facilitates the instability of this area [34,35]. Fig. 5(b) shows the surface of a NiFeP coating over anodic treated stainless steel. The morphology does not present a drastic change from the substrate, which suggests a compact coating that seeks to copy the surface of the electrode, meaning that the catalytic results that can be provided for this system are clearly associated only with the catalytic power of the deposited species. The micrograph of the NiFePZn quaternary coating obtained from a 7 mM $ZnSO_4{\cdot}7H_2O$ solution before Zn leaching is presented in Fig. 5(c) and (d) at magnifications of X2000 and X20000 respectively. At lower magnifications, it was possible to identify the valleys and peaks such as those exhibited by the substrate and NiFeP coating. However, the effect of the addition of Zn in the coating can be detected due to the formation of small cluster structures with filaments on the surface, which is not observable in the coatings without Zn. This shows that the addition of Zn promotes a notable change in the microstructure with an increase of roughness even before the leaching process.

Fig. 5(e) to (h) show the leached coating at X500, X2000 and X20000 magnifications, where some structures of three different sizes are observed. The Zn leaching process leaves the cluster structures with a brain-like morphology constituted by small plates of < 1.0 µm in size, contributing to the increase in the surface area of the electrode. In summary, at first, the macroscopic structure was generated by the anodic treatment applied to the substrate (Fig. 5(a)). Then, at intermediate level, irregularly shaped cracks and cavities appear after the electro-deposition of the NiFeP/Zn coating, resembling the surface of coral (Fig. 5(b) and (c)). Finally, it is possible to identify the formation of small clusters with an approximate size of 1.5 µm, which are distributed over the entire surface of the electrode and appear in the form of nanoplates (Fig. 5(c) and (d)). This distribution of morphologies would explain the large surface area exhibited by the NiFeP/Zn coating after Zn leaching.

To continue investigating the morphology of the coating, some analyses using the Atomic Force Microscope (AFM) were performed, the results are presented in Fig. S2, in the supporting information, and Table 2. From the AFM images the roughness values of Ra (arithmetic roughness) and Rq (quadratic roughness) for the coatings before and after leaching were obtained. The results confirm that the unleached NiFePZn coating (Fig. S2(a) and (d)) tends to be smoother and only presents cavities due to the anodic treatment of the substrate, so it only has an Ra of nearly 55 nm. An increase in average roughness up to an Ra of approximately 284 nm is then observed in the leached NiFeP/Zn coating (Fig. S2(b) and S2(e)). In addition, Fig. S2(c) and (f) show micrographs with higher magnifications of the leached coating, where the roughness generated by the nanoplates distributed on the surface is detected. These nanoplates alone have a roughness with an Ra of approximately 102 nm.

Table 2
Ra and Rq values calculated using AFM analysis of the obtained NiFePZn coating electrodeposited from a 7 mM $ZnSO_4{\cdot}7H_2O$ solution before and after Zn leaching to obtain NiFeP/Zn.

Sample	Ra (nm)	Rq (nm)
NiFePZn Before Leaching	54.975	72.031
NiFeP/Zn After Leaching 1	284.135	343.442
NiFeP/Zn After Leaching 2	101.725	122.436

A chemical characterization of NiFeP/Zn coating was carried out to complement the previous Raman spectroscopy analysis and to determine the species deposited. EDS mapping results for electrodes before and after leaching are shown in Fig. S3, in the supporting information, and the atomic percentage of the main elements of the coatings obtained is reported in Table 3. The NiFePZn (unleached) coating exhibits a high zinc content (70.90%), superior to the iron and nickel contents which do not exceed a value of 15 at% in the coating, despite the fact that the concentration of Zn in the electrodeposition bath was lower than that of Ni and Fe. Phosphorus, meanwhile, only has 3.75 at% in the coating. These results indicate the existence of an anomalous electrodeposition of Zn and Fe, because the less noble metals tend to have a greater deposition even though they have more negative standard reduction potentials than Ni (Zn= −0.7626 V vs RHE, Fe= −0.44 V vs RHE and Ni=

Table 3
Atomic percent content of the main elements presented in the NiFeP/Zn coating electrodeposited from a 7 mM $ZnSO_4{\cdot}7H_2O$ solution before and after Zn leaching, results from EDS analysis.

BEFORE LEACHING (NiFePZn)		AFTER LEACHING (NiFeP/Zn)	
Element	Atomic percent (%)	Element	Atomic percent (%)
Ni	11.60	Ni	56.20
Fe	13.74	Fe	18.82
Zn	70.90	Zn	17.33
P	3.75	P	7.65

−0.257 V vs RHE) [43]. These results differ from those of other works that used similar concentrations of Zn, Fe and Ni [25,26,44–47]. This could be related to the effect of phosphorus addition, because the P promotes different interaction during the electrodeposition of Ni-Fe systems and a local pH variation that modifies the stability of the deposited metals [21]. After the leaching process to form NiFeP/Zn coating, there was a great reduction of the Zn content in the coating, and consequently the contents of Fe, Ni and P increased. This confirms that the leaching process results not only in the generation of great surface area, but also acts as surface treatment that modifies the content of other elements present in the coating, as was established above during the Raman analysis. The chemical analysis of the EDS results also gives some explanation for the poor catalytic performance of the coating electrodeposited at the highest Zn concentration in the electrolyte bath (8.4 mM of $ZnSO_4$). Considering that most of the coating before leaching is made up of zinc, it is possible that increasing the concentration of this metal in the bath to more than 7 mM would result in the deposition of an extremely high content of Zn in the coating, which would reduce the amount Ni and Fe, thus reducing the formation of catalytic species of both these metals, which are the most active in the hydrogen and oxygen evolution reactions. Similarly, the formation of highly Zn-enriched coatings could lead to complete leaching of the catalyst, in turn leading to exposure of the stainless-steel substrate with lower active area and limited catalytic properties, as was mentioned during CV evaluation.

The diffractogram obtained of the coating electrodeposited from a 7 mM $ZnSO_4{\cdot}7H_2O$ solution before and after Zn leaching is shown in Fig. 6, along with systems such as stainless-steel and NiFeP for purposes of comparison. In all diffractograms, peaks at 2θ of 43.47°, 50.67° and 74.31° were observed, which are associated with the substrate, specifically with the austenitic phase of the stainless-steel corresponding to the planes (1 0 0), (2 0 0) and (2 2 0), respectively [48]. The theoretical pattern of this material (JCPDS 33–0397) is added to the figure for purpose of comparison. Diffractograms of NiFePZn (unleached) and NiFeP/Zn (leached) system also present several diffraction peaks that are distorted and are much wider. This effect is mainly associated with the formation of compounds with small grain sizes and the presence of an amorphous structure. The main factor responsible for the amorphization of the structure is the presence of phosphorus in the coating, which generates a distortion of the crystal structure of the formed compound when it is co-deposited with transition metals, due to the difference in the diameter of the atoms. This distortion depends on the amount of P deposited [20,49]. This was corroborated by analyzing the peak formed at 2θ = 44.8°, which can be associated with the (1 1 1) plane of FCC nickel distorted by phosphorus and which forms Ni-P [50]. This amorphous peak manages to shield the response of the peak formed by the (1 0 0) plane of the substrate. Once the Zn leaching occurs, the dissolution of Zn and part of the Fe reduces the thickness of the coating and allows a greater facility for the substrate to interact with the incident x-ray radiation to obtain a response from the plane in question. In addition, amorphization of the structure generated by the presence of phosphorus is expected and desired in the coating, because it improves the catalytic properties of the coating and its corrosion resistance. Leaching process also stimulates the formation of different amorphous compounds of Fe and Ni on the surface of the coating, which can be evidenced by several broad peaks in the diffractograms. The peaks observed at 19° and 33° are respectively associated to the planes (0 0 1) and (1 0 0) of β-$Ni(OH)_2$. In addition, the peak observed at 35° is associated to the (0 1 2) plane of α-$Ni(OH)_2$ and the plane (1 1 1) of Ni-P, as previously discussed [50,51]. Furthermore, it was possible to identify the Fe_3PO_7P (ICSD ID 84,794) compound thanks to the presence of its most characteristic peak at 28°. These results are consistent with those of Raman analysis, where the formation of nickel hydroxides on this coating was clearly identified.

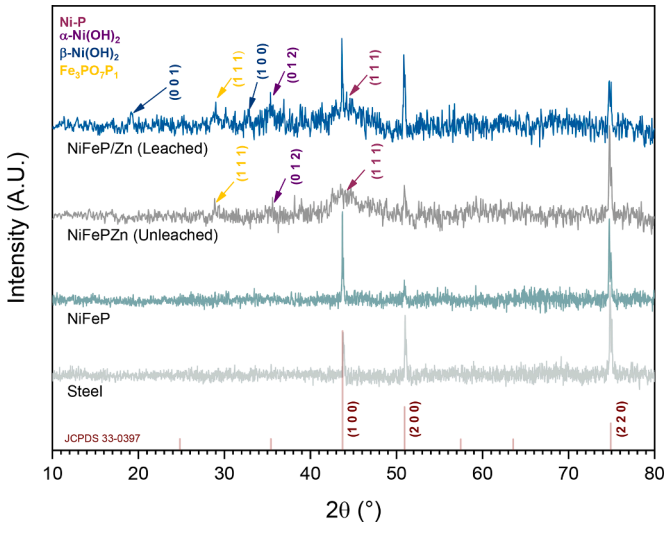

Fig. 6. X-ray diffractogram for AISI 304 steel, the ternary system NiFeP and the quaternary system NiFeP/Zn before and after Zn leaching.

X-ray photoelectron spectroscopy (XPS) measurements were carried out to complement the chemical characterization and to establish the valence states of the main elements present in the coating before and after the leaching process. The results are shown in Figs. 7. and 8. respectively. Deconvoluted spectra results from the unleached coating show that oxygen (O 1 s) has two bands (Fig. 7(b)), one at ~531.61 eV mainly associated with the dominant species of OH group, presented in the M-OH bond. This suggests the formation of a passive layer driven by the air contact after the deposition before the leaching process [52,53]. There is another band at ~533.82 eV associated to the P-O bond, possibly from bimetallic phosphates [16,54] or to the adsorbed water (H—O—H), since deposition process comes from an aqueous solution [52,53,55]. After the leaching process, the O 1 s spectra (Fig. 8(b)) shows a slight modification, evidenced by the existence of a third band at lower binding energies of ~529.17 eV. That band indicates the formation of an M-O bond in the surface [52,53,56], characteristic of a metal oxide. These results shows that leaching, in addition to the zinc remotion, helps the generation of metallic oxides, which usually act as catalyst on the surface. The band of nickel (Ni 2p) in Fig. 7(c) of the unleached sample shows a split energy of Δ~18 eV between the Ni $2p_{1/2}$ and Ni $2p_{3/2}$ spin orbits, each of which are deconvoluted into doublets corresponding to Ni^{2+} at ~855.66 eV and Ni^{3+} at ~857.34 eV for Ni $2p_{3/2}$, and Ni^{2+} at ~873.69 eV and Ni^{3+} at ~875.99 eV for Ni $2p_{1/2}$. The left bands are satellite ones [57]. The areas of the deconvoluted band show that there is some participation of Ni^{2+} in the coating, which can be related to $Ni(OH)_2$ and NiP_2 [55,58,59]. Meanwhile, Ni^{3+} can be associated to the formation of NiO_X [60]. When the coating is leached to form NiFeP/Zn, the Ni spectrum in Fig. 8(c) shows a displacement towards lower binding energies of the bands, which can be associated with the transition of $Ni(OH)_2$ species to NiO_X [60] and to NiOOH [58,61], indicating the formation of electro-catalytic compounds to HER and OER [42,62,63]. The iron spectra (Fe 2p) presented in Fig. 7(d), shows a similar behavior to the Ni spectra, with a split energy of Δ~17 eV between its spin orbits. For the Fe $2p_{3/2}$, bands at ~710.99 eV and at ~713.56 eV were deconvoluted and can be associated to Fe^{2+} and Fe^{3+} respectively. The same oxidation states are presented at ~723.82 eV and at ~726.15 eV for the $2p_{1/2}$ spin orbit. The presence of Fe^{3+} and Fe^{2+} suggests the existence of FeOOH [64] and Fe_2O_3 [59,65,66]. Remaining bands are satellite ones, and do not provide additional information [40]. After the leaching process the iron related bands show a reduction of binding energy, associated with an enrichment of oxides species, which can be related to the transition of FeOOH to FeO [65] and the formation of Fe_3O_4, as the Raman spectra suggest. The phosphorus spectra (P 2p) presented in Fig. 7(e) shows three bands, the first at ~133.64 eV corresponds to the P $2p_{3/2}$ spin orbit, while the second at ~135.04 eV is associated to the P $2p_{1/2}$ spin orbit. The presence of these bands confirms

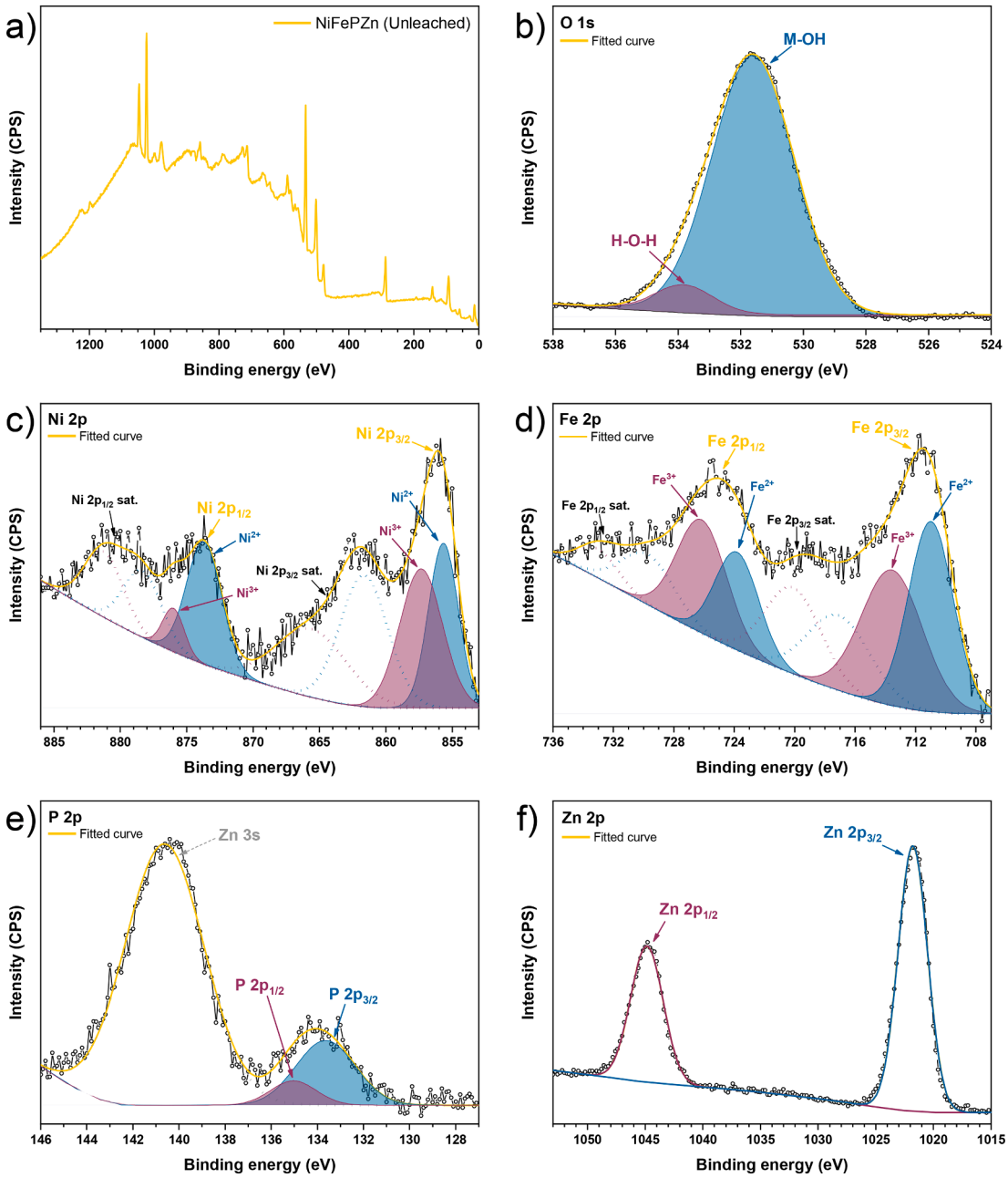

Fig. 7. XPS spectra for unleached NiFePZn coating. a) Complete spectra, b) Oxygen spectra, c) Nickel spectra, d) Iron spectra, e) Zinc spectra and f) Phosphorus spectra.

the formation of phosphides and phosphates with the deposited metals [57,67]. In the same spectrum, Fig. 7(e), the band at ~140.64 eV also appears, corresponding to the response of the Zn 3 s [67]. After the leaching treatment, in Fig. 8(e), in addition to the displacement to lower binding energies, a reduction of the intensity of the Zn 3 s band is observed, demonstrating the diminishing of this metal with this process. Finally, for the zinc spectra (Zn 2p), the two bands that appear before (Fig. 7(f)) and after (Fig. 8(f)) leaching, correspond to Zn $2p_{3/2}$ and Zn $2p_{1/2}$ respectively, with a spin orbit of Δ~23 eV. The position of these bands before leaching (at ~1021.78 eV and at ~1044.85 eV) suggests a metallic state of the zinc in the coating [68,69]. After the leaching process these bands tends to shift towards lower energies, see Fig. 8(f), probably due to the formation of ZnO, as was suggested by other works [68,70].

3.3. Electrochemical evaluation of the optimal NiFeP/Zn coating

The electrochemical behavior of the NiFeP/Zn coating obtained with 7 mM of $ZnSO_4{\cdot}7H_2O$ in the electrodeposition bath was evaluated through additional tests, to obtain more information about the kinetics of the gas evolution reactions and the stability (durability) of its catalytic behavior. Cathodic and anodic Tafel slopes obtained from potentiodynamic polarization of the coating performed in 1.0 M NaOH electrolyte are shown in Fig. 9(a) and (b), respectively. In the case of the HER reaction, Fig. 9(a), it is possible to observe that the NiFeP/Zn coating allows a reduction of the overpotential of the cathodic reaction compared to the system without Zn, indicating an improvement in the catalytic activity of the coating. Additionally, as observed in Table 4, a significant diminishing in the cathodic Tafel slope is evidenced compared to stainless steel and the NiFeP coating. This behavior is most suited to an electrolyzer operation, where high current densities are applied during

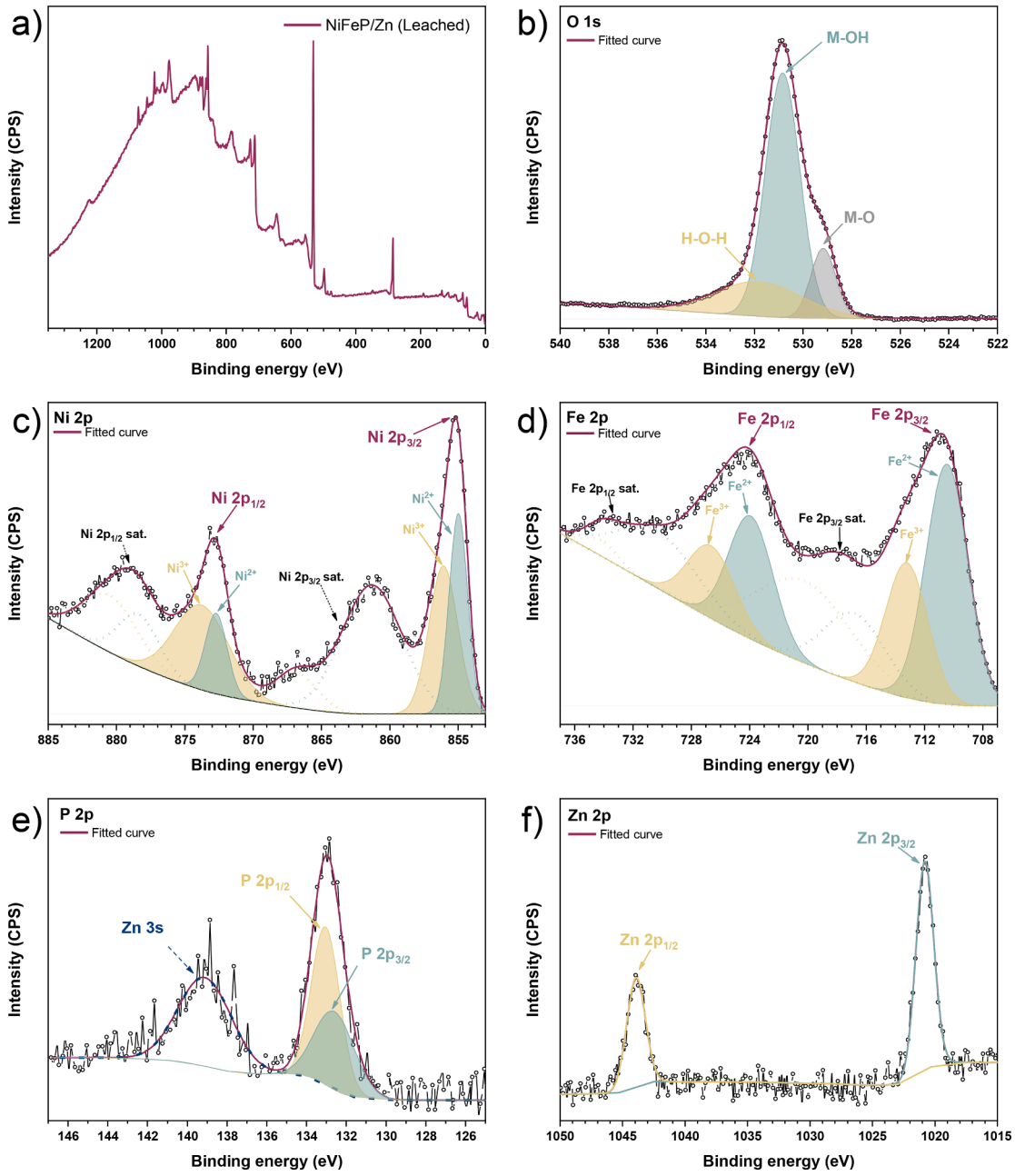

Fig. 8. XPS spectra for leached NiFeP/Zn coating. a) Complete spectra, b) Oxygen spectra, c) Nickel spectra, d) Iron spectra, e) Zinck spectra and f) Phosphorus spectra.

the generation of the H_2 gas. On the other hand, the exchange current density of the HER reaction was slightly reduced. The decrease in the exchange current is not ideal, but this could be compensated, in kinetic terms, by the diminishing of the Tafel slope, since in the LSV results presented above, the leached NiFeP/Zn coating always performed better than the other systems. Furthermore, for practical purposes in a real electrolyzer operation, it is more convenient to have a low Tafel slope, because high current densities are employed. This evaluation also allows us to identify the main mechanism of the hydrogen evolution reaction, and, in this case, the cathodic slope obtained for the quaternary system was 79 mV, which suggests that a mixed Volmer-Heyrovsky mechanism is present [71,72], possibly due to the heterogeneity of the deposited catalytic species. Oxygen evolution kinetics represented in Fig. 9(b), show two different slopes that govern the process for the three evaluated systems, one at low overpotentials in a zone between 210 mV and 310 mV, and the other at higher overpotentials between 290 mV and 420 mV. The differential anodic behavior observed at low and high overpotential is due to the formation of different catalytic compounds of nickel, which transform depending on the applied overpotential. The anodic slopes and exchange current densities for OER process are presented in Table 5. Similarly, to the HER process, the lowest values of the anodic Tafel slopes were those of the leached NiFeP/Zn quaternary system, with slopes of 25 mV for the low overpotentials and 77 mV for high overpotentials. The exchange current also presented two behaviors: in the case of the process at low overpotentials it was slightly reduced, as in the HER process, while the behavior changes at high overpotentials since the exchange current of the NiFeP/Zn system is the highest. This behavior is ideal, in conjunction with the reduction of the Tafel slope, in order to achieve higher efficient reaction kinetics for OER.

The stability of the coating was evaluated for 24 h at $|400|$ $mAcm^{-2}$, to resemble a real working operation of an electrolyzer. The chronopotentiometry curves obtained are shown in Fig. 9(c) and (d). The

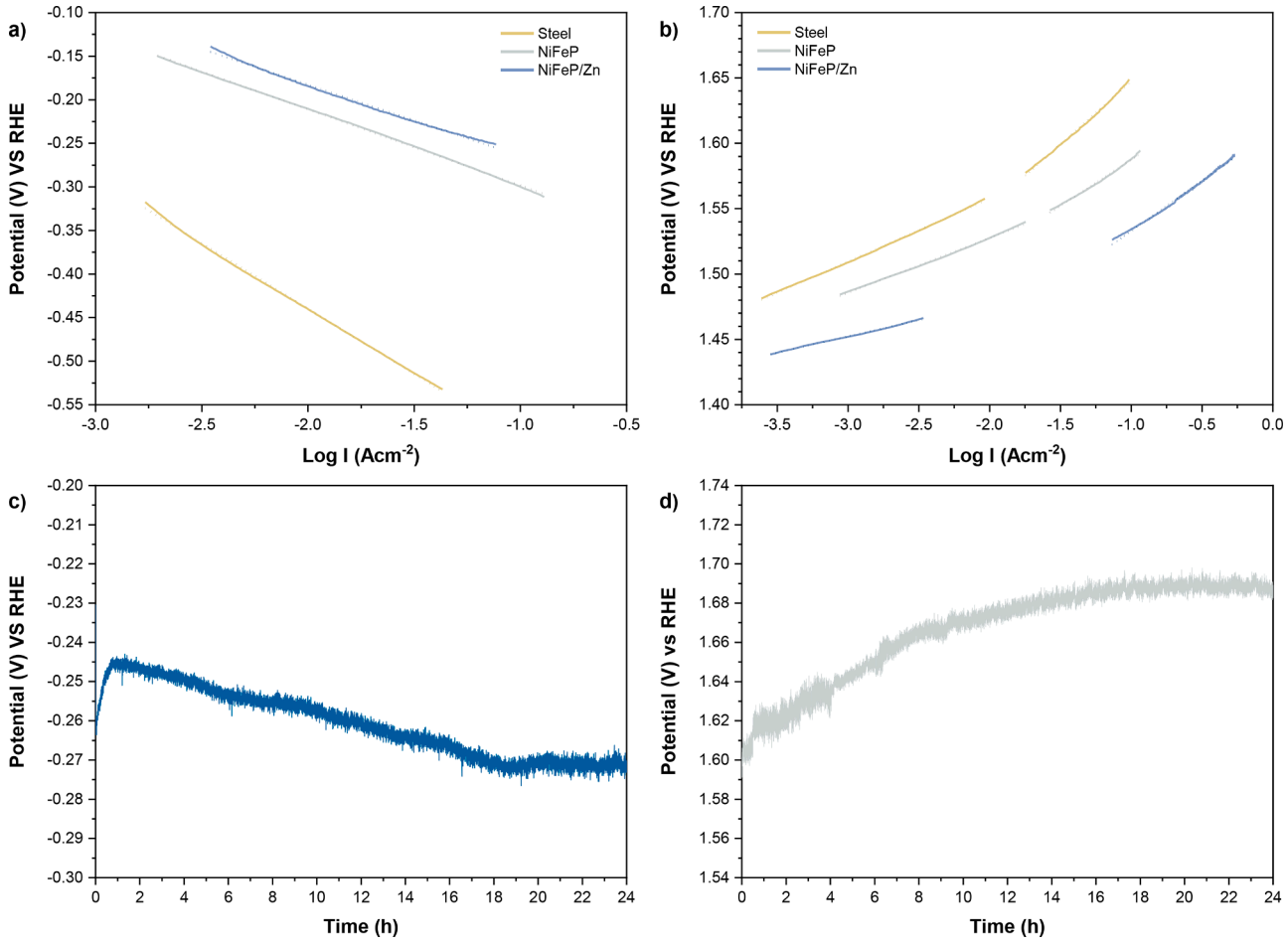

Fig. 9. Kinetics behavior of the samples analyzed from Tafel slopes and chronopotentiometry curves in 1.0 M NaOH, applying a current density of |400| mAcm^{-2}. a) Cathodic Tafel slope (HER), b) Anodic Tafel slope (OER), c) Cathodic chronopotentiometry (HER) and d) Anodic chronopotentiometry (OER).

Table 4
Tafel slopes and exchange current densities for HER.

Sample	b (mV)	Io (Acm^{-2})
Steel	158	1.68×10^{-5}
NiFeP coating [23]	93	5.52×10^{-5}
NiFeP/Zn coating	79	8.35×10^{-6}

Table 5
Tafel slopes and exchange current densities for OER.

Sample	Low overpotential		High overpotential	
	b (mV)	I_o (Acm^{-2})	b (mV)	I_o (Acm^{-2})
Steel	47	4.32×10^{-9}	114	2.81×10^{-4}
NiFeP coating [23]	43	1.03×10^{-9}	88	1.79×10^{-5}
NiFeP/Zn coating	25	1.07×10^{-12}	77	1.12×10^{-5}

observed overpotentials during the cathodic evaluation for HER varied by 30 mV and were below 275 mV, which is considered a low value for an applied current density of 400 mAcm^{-2}. Small overpotential oscillations and an initial tendency to increase were observed during the first hour of the test, but the coating reached a stable behavior around 270 mV after 18 h of polarization. During the anodic evaluation for OER, the overpotentials varied by 80 mV and exhibited a continued increase over time, with the presence of small oscillations, but it also reached a stable behavior around 1.68 V after 16 h of polarization. The increase in overpotential and the oscillations observed were associated with the constant accumulation and release of bubbles formed on the surface of the electrode. This phenomenon can lead to ohmic losses due to the increase in the system resistance with the accumulation of bubbles and due to the reduction of the active area, blocked by the same bubbles, which prevent a good interaction between the surface of the catalyst and the electrolyte. LSV measurements before and after galvanic polarization at |400| mAcm^{-2} / 24 h tests (durability tests) are shown in the Figure S4, in the supporting information. It can be seen that both LSV measurements were almost on the same curve, indicating that there is not loss of catalytic activity for the coating after high current and longtime operation. SEM images were taken after the test (Fig. S5). Small changes in the morphology respect to the pristine surface were observed, reveling some loss of the nano morphology after the lixiviation. The composition of the electrode surface was also evaluated, it is shown in Table S3 in the supporting information. It was found that the main change in the elemental metal concentration of the coating was for Zn, which is expected because Zn form soluble species in the alkaline pH of the electrolyte. However, that situation did not compromise the catalytic activity of the coating.

The results obtained during the on/off test for the evaluation of the corrosion resistance and durability of the NiFeP/Zn electrodes are shown in Fig. 10. The evaluation was performed through EIS test at the OCP after applied anodic polarization at 400 mA cm^{-2} during 2 h (OER condition) because this condition generates oxidation and could induce drastic changes of the coating. Repetitive cycles of this test (anodic galvanostatic polarization follows by EIS) were performed until reaching 24 h of evaluation. Fig. 10(a)–(c) show the Nyquist and Bode plots of the electrochemical impedance obtained for the coating at different evaluation times. After the first anodic polarization, there is a significant

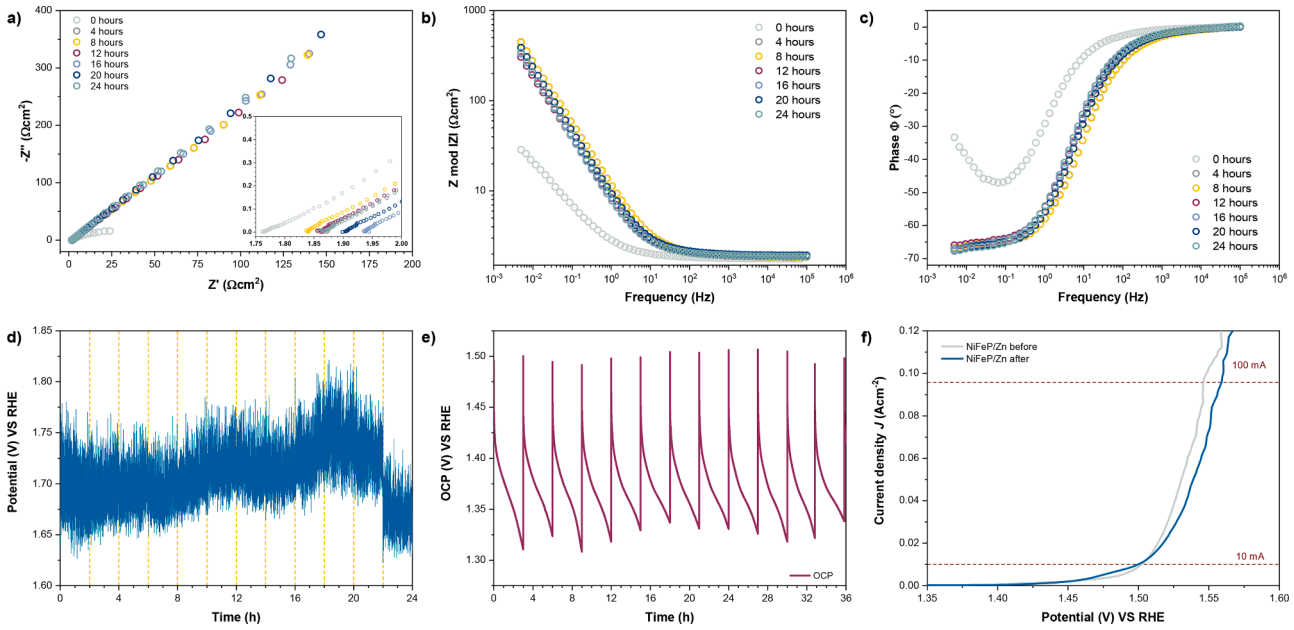

Fig. 10. Resistance to corrosion evaluation results in 1.0 M NaOH. a) EIS nyquist diagram, b) EIS bode diagram (|Z| vs Frequency), c) EIS bode diagram (Φ Vs Frequency), d) Potential variation respect time between EIS, e) OCP variation between polarizations and f) LSV results before and after corrosion evaluation.

increase in the coating impedance, after which it tends to be stable; the impedance variation is minimal from the second cycle of the test. The electrode surface during the anodic polarization on/off cycles is quite stable. Nyquist diagram shows the formation of a straight line at 45°, which is characteristic of Warburg-type semi-infinite diffusion processes. This behavior is associated with the diffusion of adsorbed oxygen from the electrode surface into the solution. In the bode spectra, an increase in the impedance of the system is observed after the first cycle of anodic polarization, while in subsequent on/off cycles no variation in impedance was observed. The increase in the impedance of the electrode after the first cycle of anodic polarization is associated with the formation of oxidation by-products of the elements that make up the coating, such as oxides, hydroxides and oxyhydroxides of Ni and Fe, which form a passive and catalytic layer on the electrode. The structure and composition of the layer has been presented in previous sections. The impedance diagrams of the system before anodic polarization (0 h), indicate the existence of two-time constants: the first at high frequencies is associated to the electrical double layer in parallel arrangement with the charge transfer resistance; and the second, at low frequencies, is probably associated with the formation of the layer of corrosion products. In the impedance performed before anodic polarization, no event associated with diffusive processes is observed. Therefore, the electrical equivalent circuits (EECs) for the electrode before and after polarization are different; both are shown in Fig. S5 in the supporting information. The EECs of Fig. S5 were used to adjust the experimental impedance values of the system. The fit results of the EIS are presented in Table S4.

The data obtained from the EIS fit confirm the stability of the coating once polarized, since all the parameters involved in the circuits remain in a similar order of magnitude during all the evaluation times. Furthermore, it can be observed that the resistance associated with the corrosion products is quite low (R_p), compared to that observed before polarization (R_{p2}). This indicates that the compounds formed on the electrode surface undergo chemical transformations and become more catalytic in nature after anodic polarization, which has already been evidenced by Raman spectroscopy and commented in previous sections. These analyzes show that the layer of corrosion products after anodic polarization is mainly constituted by nickel oxyhydroxide NiOOH, a compound that is highly catalytic for HER and OER reactions [42]. Fig. 10(d) and (e) show the variations of the overpotential with respect to time due to the applied polarization and the variation of the OCP, respectively. In the first of these, we can see a noisy behavior, where potential jumps are observed in the on/off cycles, associated with the massive production of bubbles. It is assumed that some amount of O_2 bubbles remain on the catalytic layer of the electrode after the evolution reaction during the electrolysis cycles (On condition), and later are released during the rest of time (Off condition). These events are marked with yellow lines in the graph. Despite the presence of overpotential jumps, a certain stability is observed around an average value of 1.70 V. Meanwhile, the OCP exhibits very stable behavior, which coincides with the results of the EIS, indicating that the passive layer formed does not show much variation once it is established on the surface. In each On/Off polarization cycle the OCP exhibits similar behavior; after the high polarization suffered by the coating during the On condition, a rapid fall of the OCP is observed during the Off condition to reach a stable value characteristic of the oxide species formed (NiOOH). This behavior is repeated during the cycling test, showing few changes. To complement this analysis, a LSV measurement was performed before and after completing the On/Off cycling test (24 h) to check if there were changes in the catalytic properties of the coating. The respective LSV curves performed of the NiFeP/Zn electrodes before and after the On/Off cycling test are presented in Fig. 10(f). It can be seen that the electrodes present very similar performance. At low current densities (10 mA cm^{-2}) there are no differences between the overpotentials exhibited by both electrodes, which exhibit a value close to 272 mV. At high current densities (greater than 100 mA cm^{-2}) it is possible to see a slightly larger overpotential of the NiFeP/Zn electrode after cycling test of approximately 10 mV, which still maintains acceptable ranges for the desired performance. This behavior shows that the NiFeP/Zn coating performs well in alkaline environments, is quite stable, and is resistant to corrosion generated by the oxygen evolution reaction.

3.4. Evaluation of NiFeP/Zn as bifunctional electrode for overall water splitting

A complete cell was developed to evaluate the real behavior and performance of the quaternary system NiFeP/Zn as bifunctional electrocatalyst, using the material as cathode and anode in an electrolysis cell. According to the results shown previously, a Full-Cell acting like an

electrolyzer using the bifunctional material as the respective electrodes would requires a potential difference of 1.65 V to start the water splitting and thus produce hydrogen and oxygen at a current density of 10 mA cm^{-2}. This potential is a reference value but does not include losses associated with electrical contact and wire resistances and ohmic potential drops in the electrolyte. Consequently, it is necessary to carry out a complete cell polarization curve in order to verify the theoretical performance. A triplicate evaluation of LSV was carried out to obtain statistically representative behavior, this result is shown in Fig. 11. Full-Cell potentials obtained at current densities of 10 mA cm^{-2} and 100 mA cm^{-2} were 1.65 V and 1.83 V, respectively. These overpotential values suggest correct calculation for the overall water splitting and shows good repeatability of the electrode performance. The result obtained in this research shows overpotential of Full-Cell equal to 1.65 V for overall water splitting. This demonstrates promising performance of electrolyzers, which can be constructed using the developed catalytic coatings of NiFeP/Zn, in comparison with previous reports of more expensive and elaborate electrodes, like 1.64 V for Ni-P/NF [73], 1.67 V for Ni-Fe-S [74], 1.68 V for Co-Mn carbonate hydroxide [75], 1.68 V for MoS2@-Ni0.96S [76], 1.73 V for FeSe2/NF [77], 1.73 V CoFeP/CNT [42]. Also a work reported the modification of the stainless steel surface (SSM-AR-SSM-A) achieving a voltage of 1.78 V [78]. Nevertheless, a recent developed ternary coating Ni_2P/NiMoP on NF shown excellent performance for the HER, like 1.52 V at 10 mA cm^{-2} and 1.68 at 100 mA cm^{-2} [79], showing that there is still room for improvement in future researches.

4. Conclusion

Nanostructured and reproducible NiFeP/Zn coatings were developed as bifunctional catalysts for electrochemical water splitting. The NiFeP/Zn coating was deposited on anodic-treated AISI 304 stainless-steel, after which the leaching process was used to remove part of Zn, allowing a high active surface area of the electrodes. Zn leaching process also works as an aging process that forms catalytic species such as NiOOH on the surface and establishes a convenient ratio between Ni and Fe. The optimal catalytic coating was that obtained in the electrolytic bath containing 7 mM of Zn, which corresponds to a coating composition of 56.20% Ni, 18.82% Fe, 7.65% P and 17.33% Zn, after leaching process. These effects resulted in the achievement of low overpotentials for HER and OER reactions, specifically 163 mV and 262 mV, respectively, at a current density of 10 mA cm^{-2}. SEM and AFM characterizations show that leached electrodes have a diversified surface with different structures and coral-like distributions that enhance the catalytic behavior. Raman spectra, XRD and XPS show that different amorphous Ni oxides and hydroxides participate on the surface of the leached electrodes, and when the electrode is anodically polarized additional nickel oxyhydroxide is also formed. NiFeP/Zn coating showed a good performance after cyclic corrosion test and the passive layer formed is very stable. Finally, a Full-Cell test using the NiFeP/Zn coating as bifunctional electrodes displays a very low overpotential equal to 1.65 V at 10 mA cm^{-2} for overall water splitting.

Credit authorship contribution statement

Jhaniel Osorio: Investigation, Methodology, Writing. Santiago Cartagena: Conceptualization, Investigation, Methodology, Review & editing. Jorge Calderón: Conceptualization, methodology, project administration, funding acquisition, supervision, and writing - review & editing.

Declaration of Competing Interest

The authors declare that they have no known competing financial interests or personal relationships that could have appeared to influence the work reported in this paper.

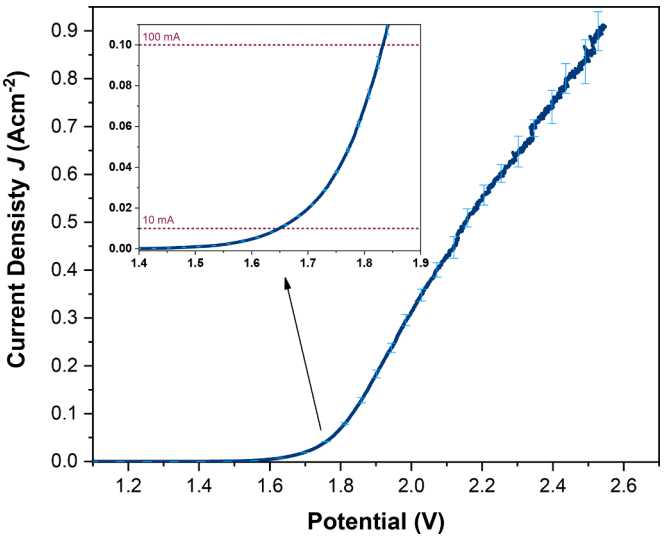

Fig. 11. LSV curve of Full-Cell, evaluating the NiFeP/Zn coating as bifunctional electrode for overall water splitting in 1.0 M NaOH.

Data availability

The authors declare that data of current manuscript are available on reasonable request from the interested.

Acknowledgments

The authors would like to thank Colombian Ministry of Science, Technology and Innovation “Minciencias” for financial support through the scientific project contract no 177-2021.

Supplementary materials

Supplementary material associated with this article can be found, in the online version, at doi:10.1016/j.electacta.2023.142299.

References

[1] X. Tan, L. Han, X. Zhang, W. Zhou, W. Li, Y. Qian, A review of current air quality indexes and improvements under the multi-contaminant air pollution exposure, J. Environ. Manage. 279 (2021), 111681, https://doi.org/10.1016/j.jenvman.2020.111681. July 2020.
[2] A. Godula-Jopek, Hydrogen Production by Electrolysis, Wiley - VCH, 2015.
[3] K. Zeng and M. Eng, “Improvements and Optimisation of Water Electrolysis for Hydrogen Production,” 2012.
[4] W. Liu, H. Zuo, J. Wang, Q. Xue, B. Ren, F. Yang, The production and application of hydrogen in steel industry, Int. J. Hydrogen Energy 46 (17) (2021) 10548–10569, https://doi.org/10.1016/j.ijhydene.2020.12.123.
[5] S. Griffiths, B.K. Sovacool, J. Kim, M. Bazilian, J.M. Uratani, Industrial decarbonization via hydrogen: a critical and systematic review of developments, socio-technical systems and policy options, Energy Res. Soc. Sci. 80 (2021), 102208, https://doi.org/10.1016/j.erss.2021.102208 no. August.
[6] M. Zier, P. Stenzel, L. Kotzur, D. Stolten, A review of decarbonization options for the glass industry, Energy Convers. Manag. X 10 (no. May) (2021), 100083, https://doi.org/10.1016/j.ecmx.2021.100083.
[7] K. Zeng, D. Zhang, Recent progress in alkaline water electrolysis for hydrogen production and applications, Prog. Energy Combust. Sci. 36 (3) (2010) 307–326, https://doi.org/10.1016/j.pecs.2009.11.002.
[8] D. Jang, W. Choi, H.S. Cho, W.C. Cho, C.H. Kim, S. Kang, Numerical modeling and analysis of the temperature effect on the performance of an alkaline water electrolysis system, J. Power Sources 506 (no. May) (2021), 230106, https://doi.org/10.1016/j.jpowsour.2021.230106.
[9] K. Torii, M. Kodama, S. Hirai, Three-dimensional coupling numerical simulation of two-phase flow and electrochemical phenomena in alkaline water electrolysis, Int. J. Hydrog. Energy 46 (71) (2021) 35088–35101, https://doi.org/10.1016/j.ijhydene.2021.08.101.
[10] R. Phillips, W.J.F. Gannon, C.W. Dunnill, Alkaline Electroly. (25) (2020).

[11] I. Flis-Kabulska, J. Flis, Electroactivity of Ni–Fe cathodes in alkaline water electrolysis and effect of corrosion, Corros. Sci. 112 (2016) 255–263, https://doi.org/10.1016/j.corsci.2016.07.017.

[12] F. Safizadeh, G. Houlachi, E. Ghali, Electrocatalytic activity and corrosion behavior of FeMo and FeMoP coatings employed as cathode material for alkaline water electrolysis, Int. J. Hydrog. Energy 43 (16) (2018) 7938–7945, https://doi.org/10.1016/j.ijhydene.2018.03.071.

[13] A.M. Fundo, L.M. Abrantes, Electrocatalytic behavior of electroless Ni-P alloys for the oxygen evolution reaction, Russ. J. Electrochem. 42 (12) (2006) 1291–1297, https://doi.org/10.1134/S1023193506120044.

[14] V. Torabinejad, M. Aliofkhazraei, S. Assareh, M.H. Allahyarzadeh, A. S. Rouhaghdam, Electrodeposition of Ni-Fe alloys, composites, and nano coatings–A review, J. Alloy. Compd. 691 (2017) 841–859, https://doi.org/10.1016/j.jallcom.2016.08.329.

[15] W.-K. Gao, et al., Optimized bimetallic nickel-iron phosphides with rich defects as enhanced electrocatalysts for oxygen evolution reaction, J. Colloid Interface Sci. 537 (2019) 11–19, https://doi.org/10.1016/j.jcis.2018.10.099.

[16] Y. Li, C. Zhao, Enhancing Water Oxidation Catalysis on a Synergistic Phosphorylated NiFe Hydroxide by Adjusting Catalyst Wettability, ACS Catal. 7 (4) (2017) 2535–2541, https://doi.org/10.1021/acscatal.6b03497. Apr.

[17] F. Diao, et al., Bifunctional and Self-Supported NiFeP-Layer-Coated NiP Rods for Electrochemical Water Splitting in Alkaline Solution, ACS Appl. Mater. Interface. 13 (20) (2021) 23702–23713, https://doi.org/10.1021/acsami.1c03089.

[18] J. Tang, B. Mu, L. Zong, A. Wang, One-step synthesis of magnetic attapulgite/carbon supported NiFe-LDHs by hydrothermal process of spent bleaching earth for pollutants removal, J. Clean. Prod. 172 (2018) 673–685, https://doi.org/10.1016/j.jclepro.2017.10.181.

[19] W. Tang, S. Zuo, J. Wang, Y. Mi, Z. Chen, A NiFe-Based Hierarchically Structured 3D Electrode by Hydrothermal Deposition for Highly Efficient Water Oxidation, Electrochim. Acta 247 (2017) 835–842, https://doi.org/10.1016/j.electacta.2017.07.075.

[20] K. Sridharan, K. Sheppard, Crystallization of amorphous iron-nickel-phosphorus alloys prepared by electrodeposition, J. Mater. Process. Technol. 68 (2) (1997) 109–116, https://doi.org/10.1016/S0924-0136(96)00017-9.

[21] K. Sridharan, K. Sheppard, Electrodeposition of amorphous iron-nickel-phosphorus alloy coatings, Trans. IMF 72 (4) (1994) 153–158, https://doi.org/10.1080/00202967.1994.11871044. Jan.

[22] A. Lelevic, F.C. Walsh, Electrodeposition of Ni-P alloy coatings: a review, Surf. Coating. Technol. 369 (2019) 198–220, https://doi.org/10.1016/j.surfcoat.2019.03.055, no. March.

[23] S. Cartagena, F.E. Bedoya-Lora, J.A. Calderón, Enhancement of anodically treated stainless steel by NiFeP-catalyst electrodeposition as bifunctional electrodes for water electrolysis, J. Electrochem. Soc. 169 (4) (2022) 44501, https://doi.org/10.1149/1945-7111/ac5ff1.

[24] M.V. Ananth, N.V. Parthasaradhy, Hydrogen evolution characteristics of electrodeposited Ni-Zn-Fe coatings in alkaline solutions, Int. J. Hydrog. Energy 22 (8) (1997) 747–751, https://doi.org/10.1016/s0360-3199(96)00206-6.

[25] W.A. Badawy, H. Nady, G.M. Abd El-Hafez, Electrodeposited Zn-Ni alloys as promising catalysts for hydrogen production-preparation, characterization and electro-catalytic activity, J. Alloy. Compd. 699 (2017) 1146–1156, https://doi.org/10.1016/j.jallcom.2016.12.228.

[26] I. Herraiz-Cardona, E. Ortega, L. Vázquez-Gómez, V. Pérez-Herranz, Electrochemical characterization of a NiCo/Zn cathode for hydrogen generation, Int. J. Hydrog. Energy 36 (18) (2011) 11578–11587, https://doi.org/10.1016/j.ijhydene.2011.06.067.

[27] C. Roy, et al., Impact of nanoparticle size and lattice oxygen on water oxidation on NiFeOxHy, Nat. Catal. 1 (11) (2018) 820–829, https://doi.org/10.1038/s41929-018-0162-x.

[28] S.Y. Lim, S. Park, S.W. Im, H. Ha, H. Seo, K.T. Nam, Chemically deposited amorphous Zn-doped NiFeO xH y for enhanced water oxidation, ACS Catal. 10 (1) (2020) 235–244, https://doi.org/10.1021/acscatal.9b03544.

[29] V. Bachvarov, E. Lefterova, R. Rashkov, Electrodeposited NiFeCo and NiFeCoP alloy cathodes for hydrogen evolution reaction in alkaline medium, Int. J. Hydrog. Energy 41 (30) (2016) 12762–12771, https://doi.org/10.1016/j.ijhydene.2016.05.164.

[30] Q. Yang, C. Lv, Z. Huang, C. Zhang, Amorphous film of ternary Ni–Co–P alloy on Ni foam for efficient hydrogen evolution by electroless deposition, Int. J. Hydrog. Energy 43 (16) (2018) 7872–7880, https://doi.org/10.1016/j.ijhydene.2018.03.003.

[31] S. Sivakumar, et al., Fabrication of nickel-yttria stabilized zirconia 3D micro-pattern by atmospheric plasma spray as a dual-functional electrocatalyst for overall water splitting applications in alkaline medium, J. Power Source. 473 (2020), 228526, https://doi.org/10.1016/j.jpowsour.2020.228526.

[32] P. Ramakrishnan, S. Jo, N. Pitipuech, J.I. Sohn, Bifunctionality behavior of phase controlled nickel selenides in alkaline water electrolysis application, Electrochim. Acta 354 (2020), 136742, https://doi.org/10.1016/j.electacta.2020.136742.

[33] W. Zheng, M. Liu, L.Y.S. Lee, Best practices in using foam-type electrodes for electrocatalytic performance benchmark, ACS Energy Lett. 5 (10) (2020) 3260–3264, https://doi.org/10.1021/acsenergylett.0c01958. Oct.

[34] P. Scheffel, et al., Anodización de aceros inoxidables como tratamiento superficial para la obtención de estructuras porosas, Rev. Latinoam. Metal. y Mater. 34 (2) (2014) 189–195.

[35] A. Bervian, et al., The influence of the glycerin concentration on the porous structure of ferritic stainless steel obtained by anodization, Dyna (Medellin) 82 (2015) 46–52, https://doi.org/10.15446/dyna.v82n190.42638, scieloco.

[36] L.M. Da Silva, L.A. De Faria, J.F.C. Boodts, Determination of the morphology factor of oxide layers, Electrochim. Acta 47 (3) (2001) 395–403, https://doi.org/10.1016/S0013-4686(01)00738-1.

[37] G. Spinolo, S. Ardizzone, S. Trasatti, Surface characterization of Co3O4 electrodes prepared by the sol-gel method, J. Electroanal. Chem. 423 (1997) 49–57.

[38] R. Solmaz, G. Kardaş, Hydrogen evolution and corrosion performance of NiZn coatings, Energy Convers. Manag. 48 (2) (2007) 583–591, https://doi.org/10.1016/j.enconman.2006.06.004.

[39] C. Kjartansdóttir, M. Caspersen, S. Egelund, P. Møller, Electrochemical investigation of surface area effects on PVD Al-Ni as electrocatalyst for alkaline water electrolysis, Electrochim. Acta 142 (2014) 324–335, https://doi.org/10.1016/j.electacta.2014.07.061.

[40] R. Nandan, A. Gautam, K.K. Nanda, Anthocephalus cadamba shaped FeNi encapsulated carbon nanostructures for metal-air batteries as a resilient bifunctional oxygen electrocatalyst, J. Mater. Chem. A 6 (41) (2018) 20411–20420, https://doi.org/10.1039/c8ta05822a.

[41] D.L.A. de Faria, S.V. Silva, and M.T. de Oliveira, "Raman microspectroscopy of some iron oxides and oxyhydroxides," *J. Raman Spectrosc.*, vol. 28, no. 11, pp. 873–878, Nov. 1997, https://doi.org/https://doi.org/10.1002/(SICI)1097-4555(199711)28:11<873::AID−JRS177>3.0.CO;2-B.

[42] M.W. Louie, A.T. Bell, An investigation of thin-film Ni-Fe oxide catalysts for the electrochemical evolution of oxygen, J. Am. Chem. Soc. 135 (33) (2013) 12329–12337, https://doi.org/10.1021/ja405351s.

[43] A.J. Bard, L.R. Faulkner, Electrochemical Methods Fundamentals and Applications, 2nd Edi., John Wiley & Sons, Inc., 2001 https://doi.org/10.1016/B978-0-12-381373-2.00056-9.

[44] B. Li, D. Li, W. Xia, W. Zhang, Synthesis and characterization of a novel Zn-Ni and Zn-Ni/Si 3 N 4 composite coating by pulse electrodeposition, Appl. Surf. Sci. 458 (2018) 665–677, https://doi.org/10.1016/j.apsusc.2018.07.146. June.

[45] A.C. Hegde, K. Venkatakrishna, N. Eliaz, Electrodeposition of Zn-Ni, Zn-Fe and Zn-Ni-Fe alloys, Surf. Coating. Technol. 205 (7) (2010) 2031–2041, https://doi.org/10.1016/j.surfcoat.2010.08.102.

[46] M. Rahsepar, M.E. Bahrololoom, Study of surface roughness and corrosion performance of Ni/Zn-Fe and Zn-Fe/Ni compositionally modulated multilayer coatings, Surf. Coating. Technol. 204 (5) (2009) 580–585, https://doi.org/10.1016/j.surfcoat.2009.08.036.

[47] E.C.S. Transactions and T.E. Society, "EIS Charaterization of Ni/Zn and Ni-Co/Zn Satinless Steel Bases Electrodeposits for the Hydrogen Evolution Reaction," vol. 25, no. 32, pp. 79–91, 2010.

[48] M.-S. Balogun, et al., Cost-effective alkaline water electrolysis based on nitrogen- and phosphorus-doped self-supportive electrocatalysts, Adv. Mater. 29 (34) (2017), 1702095, https://doi.org/10.1002/adma.201702095. Sep.

[49] J. Lian, Y. Wu, H. Zhang, S. Gu, Z. Zeng, X. Ye, One-step synthesis of amorphous Ni–Fe–P alloy as bifunctional electrocatalyst for overall water splitting in alkaline medium, Int. J. Hydrog. Energy 43 (29) (2018) 12929–12938, https://doi.org/10.1016/j.ijhydene.2018.05.107.

[50] M. Crobu, A. Scorciapino, B. Elsener, A. Rossi, The corrosion resistance of electroless deposited nano-crystalline Ni-P alloys, Electrochim. Acta 53 (8) (2008) 3364–3370, https://doi.org/10.1016/j.electacta.2007.11.071.

[51] S.A. Sreenavya, B.T. Baskaran, G.V. Ganesh, S.D. Sharma, N. Kulal, S.A. Sakthivel, Framework of ruthenium-containing nickel hydrotalcite-type material: preparation, characterisation, and its catalytic application, RSC Adv. 8 (44) (2018) 25248–25257, https://doi.org/10.1039/c8ra03506g.

[52] H. Zhang, et al., Bifunctional heterostructure assembly of NiFe LDH nanosheets on NiCoP nanowires for highly efficient and stable overall water splitting, Adv. Funct. Mater. 28 (14) (2018) 1–10, https://doi.org/10.1002/adfm.201706847.

[53] Thermo Scientific XPS, "XPS Interpretation of Oxygen".

[54] J. Xing, H. Li, M. Ming-Cheng Cheng, S.M. Geyer, K.Y.S. Ng, Electro-synthesis of 3D porous hierarchical Ni-Fe phosphate film/Ni foam as a high-efficiency bifunctional electrocatalyst for overall water splitting, J. Mater. Chem. A 4 (36) (2016) 13866–13873, https://doi.org/10.1039/c6ta05952j.

[55] L. Tian, et al., Ultrathin wrinkled NiFeP nanosheets enable efficient oxygen evolution electrocatalysis, J. Taiwan Inst. Chem. Eng. 97 (2019) 200–206, https://doi.org/10.1016/j.jtice.2019.01.023.

[56] Y. Li, C. Zhao, Iron-doped nickel phosphate as synergistic electrocatalyst for water oxidation, Chem. Mater. 28 (16) (2016) 5659–5666, https://doi.org/10.1021/acs.chemmater.6b01522. Aug.

[57] R.-Q. Li, et al., Monolithic electrode integrated of ultrathin NiFeP on 3D strutted graphene for bifunctionally efficient overall water splitting, Nano Energy 58 (2019) 870–876, https://doi.org/10.1016/j.nanoen.2019.02.024.

[58] S.H. Ahn, A. Manthiram, Direct growth of ternary Ni–Fe–P porous nanorods onto nickel foam as a highly active, robust bi-functional electrocatalyst for overall water splitting, J. Mater. Chem. A 5 (6) (2017) 2496–2503, https://doi.org/10.1039/C6TA10509B.

[59] Y. Du, Z. Li, Y. Liu, Y. Yang, L. Wang, Nickel-iron phosphides nanorods derived from bimetallic-organic frameworks for hydrogen evolution reaction, Appl. Surf. Sci. 457 (2018) 1081–1086, https://doi.org/10.1016/j.apsusc.2018.06.167. April.

[60] Thermo Scientific XPS, "XPS Interpretation of Nickel".

[61] D. Koushik, et al., Plasma-assisted atomic layer deposition of nickel oxide as hole transport layer for hybrid perovskite solar cells, J. Mater. Chem. C 7 (40) (2019) 12532–12543, https://doi.org/10.1039/c9tc04282b.

[62] R. Badrnezhad, F. Nasri, H. Pourfarzad, S.K. Jafari, Effect of iron on Ni–Mo–Fe composite as a low-cost bifunctional electrocatalyst for overall water splitting, Int. J. Hydrog. Energy 46 (5) (2021) 3821–3832, https://doi.org/10.1016/j.ijhydene.2020.10.174.

[63] J. Mohammed-Ibrahim, X. Sun, Recent progress on earth abundant electrocatalysts for hydrogen evolution reaction (HER) in alkaline medium to achieve efficient water splitting – a review, J. Energy Chem. 34 (2019) 111–160, https://doi.org/10.1016/j.jechem.2018.09.016.
[64] H. Liang, et al., Amorphous NiFe-OH/NiFeP electrocatalyst fabricated at low temperature for water oxidation applications, ACS Energy Lett. 2 (5) (2017) 1035–1042, https://doi.org/10.1021/acsenergylett.7b00206. May.
[65] Thermo Scientific XPS, "XPS Interpretation of Iron".
[66] X. Cheng, et al., A strongly coupled 3D ternary Fe2O3@Ni2P/Ni(PO3)2 hybrid for enhanced electrocatalytic oxygen evolution at ultra-high current densities, J. Mater. Chem. A 7 (3) (2019) 965–971, https://doi.org/10.1039/C8TA11223A.
[67] Thermo Scientific XPS, "XPS Interpretation of Phosphorus".
[68] M.C. Biesinger, L.W.M. Lau, A.R. Gerson, R.S.C. Smart, Resolving surface chemical states in XPS analysis of first row transition metals, oxides and hydroxides: Sc, Ti, V, Cu and Zn, Appl. Surf. Sci. 257 (3) (2010) 887–898, https://doi.org/10.1016/j.apsusc.2010.07.086.
[69] Thermo Scientific XPS, "XPS Interpretation of Zinc".
[70] D. Xu, D. Fan, W. Shen, Catalyst-free direct vapor-phase growth of Zn1-xCuxO micro-cross structures and their optical properties, Nanoscale Res. Lett. 8 (1) (2013) 1–9, https://doi.org/10.1186/1556-276X-8-46.
[71] N. Mahmood, Y. Yao, J.W. Zhang, L. Pan, X. Zhang, J.J. Zou, Electrocatalysts for Hydrogen Evolution in Alkaline Electrolytes: mechanisms, Challenges, and Prospective Solutions, Adv. Sci. 5 (2) (2018), https://doi.org/10.1002/advs.201700464.
[72] A. Lasia, Mechanism and kinetics of the hydrogen evolution reaction, Int. J. Hydrog. Energy 44 (36) (2019) 19484–19518, https://doi.org/10.1016/j.ijhydene.2019.05.183.
[73] X. Wang, W. Li, D. Xiong, L. Liu, Fast fabrication of self-supported porous nickel phosphide foam for efficient, durable oxygen evolution and overall water splitting, J. Mater. Chem. A 4 (15) (2016) 5639–5646, https://doi.org/10.1039/c5ta10317g.
[74] J. Li, Z.-.Y. Wang, N. Deng, C.-.X. Li, Z.-.G. Guo, J.-.B. He, In situ formation of a nickel-iron-sulfur bifunctional catalyst within a porous polythiophene coating for water electrolysis, Int. J. Hydrog. Energy (2022), https://doi.org/10.1016/j.ijhydene.2022.03.242 no. xxxx.
[75] T. Tang, et al., Electronic and morphological dual modulation of cobalt carbonate hydroxides by Mn doping toward highly efficient and stable bifunctional electrocatalysts for overall water splitting, J. Am. Chem. Soc. 139 (24) (2017) 8320–8328, https://doi.org/10.1021/jacs.7b03507.
[76] S. Liu, B. Li, S.V. Mohite, P. Devaraji, L. Mao, R. Xing, Ultrathin MoS2 nanosheets in situ grown on rich defective Ni0.96S as heterojunction bifunctional electrocatalysts for alkaline water electrolysis, Int. J. Hydrog. Energy 45 (55) (2020) 29929–29937, https://doi.org/10.1016/j.ijhydene.2020.08.034.
[77] C. Panda, et al., From a molecular 2Fe-2Se precursor to a highly efficient iron diselenide electrocatalyst for overall water splitting, Angew. Chemie Int. Ed. 56 (35) (Aug. 2017) 10506–10510, https://doi.org/10.1002/anie.201706196.
[78] J. Ekspong, T. Wågberg, Stainless steel as A Bi-functional electrocatalyst-A top-down approach, Mater. (Basel, Switzerland) 12 (13) (2019), https://doi.org/10.3390/ma12132128. Jul.
[79] T. Wang, X. Cao, L. Jiao, Ni2P/NiMoP heterostructure as a bifunctional electrocatalyst for energy-saving hydrogen production, eScience 1 (1) (2021) 69–74, https://doi.org/10.1016/j.esci.2021.09.002.